UNIVERSIDADE DE LISBOA
Faculdade de Ciências
Departamento de Física

THE DIFFERENTIAL EVOLUTION OF HOT- AND COLD-DUST IN GALAXIES IN THE LAST 7.5 GYR

Mestrado em Física
Especialização em Astrofísica e Cosmologia

Joana Patricia Marques Oliveira

Dissertação orientada por:
Prof. Doutor José Manuel Lourenço Coutinho Afonso
Doutor Hugo Galhardas Messias

2016

Acknowledgments

There are so many people I wish to thank for all the support throughout the journey that led to this point, the moment where I am closing a chapter of my life, and hopefully, beginning a new one. Unfortunately, I won't be able to list everyone here, but I still want to leave some thank you notes.

First, I wish to thank my supervisors, Dr José Afonso and Dr Hugo Messias, for allowing me to work under them. I also want to leave a special thank you to Dr Hugo Messias for his infinite patience towards me.

Thank you, João Retrê, for all the support and opportunities you've given and shown me during these 6 years, and hopefully many more to come.

I also want to thank Dr Pedro Machado for showing me an area of Astrophysics I never knew I would be interested in and passionate about.

Diogo Pereira, thank for your love and patience, for all our moments together and for just being you.

Vanessa Pires, thank you for putting up with me for all these years (12, or 13?) and for all the laughs, gossip, and general craziness.

Thank you, João Oliveira, for making a wager with me, stating that you would finish your Bachelor Degree when I concluded my Dissertation.

And, finally, a special thank you to my parents, for believing in me, and for all their unconditional support.

The author thanks the COSMOS team for the multi-wavelength catalog which is the base of this study, and the NASA/IPAC Infrared Science Archive, operated by the Jet Propulsion Laboratory, California Institute of Technology, under contract with the National Aeronautics and Space Administration.

This work is based on observations made with the *Spitzer* Space Telescope, which is operated by the Jet Propulsion Laboratory, California Institute of Technology under a contract with NASA, and with ESA's *Herschel* Space Observatory, in particular employing *Herschel*'s large telescope and powerful science payload to do photometry using the PACS and SPIRE instruments.

PACS has been developed by a consortium of institutes led by MPE (Germany) and including UVIE (Austria); KU Leuven, CSL, IMEC (Belgium); CEA, LAM (France); MPIA (Germany); INAF-IFSI/OAA/OAP/OAT, LENS, SISSA (Italy); IAC (Spain). This development has been supported by the funding agencies BMVIT (Austria), ESA-PRODEX (Belgium), CEA/CNES (France), DLR (Germany), ASI/INAF (Italy), and CICYT/MCYT (Spain).

SPIRE has been developed by a consortium of institutes led by Cardiff University (UK) and including Univ. Lethbridge (Canada); NAOC (China); CEA, LAM (France); IFSI, Univ. Padua (Italy); IAC (Spain); Stockholm Observatory (Sweden); Imperial College London, RAL, UCL-MSSL, UKATC, Univ. Sussex (UK); and Caltech, JPL, NHSC, Univ. Colorado (USA). This development has been supported by national funding agencies: CSA (Canada); NAOC (China); CEA, CNES, CNRS (France); ASI (Italy); MCINN (Spain); SNSB (Sweden); STFC, UKSA (UK); and NASA (USA).

This research has made use of data from the HerMES project. HerMES is a *Herschel* Key Programme utilizing Guaranteed Time from the SPIRE instrument team, ESAC scientists and a mission scientist. The HerMES data was accessed through the *Herschel* Database in Marseille (HeDaM) operated by CeSAM and hosted by the Laboratoire d'Astrophysique de Marseille.

The author acknowledges the use of Python, Topcat, and SAOImage DS9.

Abstract

The study of dust is crucial for the study of galaxies since it reradiates in the infrared the ultraviolet and optical radiation originating from stellar activity. A dust grain equilibrates to a temperature that is dependent of the intensity of its local radiation field, and also depends on the grain's optical properties. The heating of dust grains is done primarily by absorption of starlight, however, light from the accretion disk around a super-massive black-hole in an Active Galactic Nucleus is also an important mechanism for the heating of dust.

While understanding dust throughout cosmic time, most studies base their assumptions on far-infrared wavelengths, since that is where most of the energy resides, inferring the near- and mid-infrared from local relations or even neglecting those spectral regimes altogether. However, these spectral regimes may play a role in the regions closer to the heating sources and, therefore, may not evolve the same way as the dust radiating in the far-infrared.

This study aims to confirm a result obtained in Messias et al. (2013), where they found a clear difference between the luminosity density evolution at near-infrared wavelengths and that at far-infrared ones as reported in the literature. The goal is to verify if this result is due to a differential evolution of hot- and cold-dust, or an effect of cosmic variance. In order to address this, a direct comparison ought to be done for the same sample, which is what is pursued in this dissertation with the Cosmological Evolution Survey.

The first course of action was to characterize the far-infrared properties of the sample depending on spectral type and distance in order to assess their evolution. Luminosity density functions were then obtained, enabling a characterization of

the sample incompleteness and consequent correction of the overall luminosity density of a given population. With these results and those from Messias et al. (2013) in hand, the evolution with cosmic time of far-infrared-to-near-infrared luminosity density ratio was obtained. The results obtained to not corroborate the results in Messias et al. (2013). However, it is found that the far-infrared-to-near-infrared luminosity density ratio correlates with luminosity. Since the lowest redshift intervals may be highly affected by cosmic variance, a confirmation of these results in a wider area field is needed to allow lower statistical errors and confirm or refute the results.

Keywords: Dust, Infrared, Galaxies, Evolution, Luminosity Density.

Resumo

Observações no infravermelho a partir da Terra sempre enfrentaram o obstáculo da opacidade da atmosfera. Como tal, evidências para a existência da poeira surgiram de observações no ótico, no ano 1930, através do avermelhamento de galáxias. Desde 1983, diversas missões foram enviadas para o espaço, após clara necessidade de observações no infravermelho. É agora conhecido que o estudo da poeira é crucial para o estudo de galáxias pois absorve radiação ultravioleta originária de atividade estelar e reradia-a no infravermelho. É estimado que, pelo menos, 30% da energia emitida como luz estelar no Universo é reradiada por poeira no infravermelho.

A poeira pode ser formada por estrelas do Ramo Assintótico Gigante, ou por Supernovas. Porém, estes mecanismos produzem uma quantidade de poeira aquém daquela observada em Objetos Quasi-Estelares a desvios para o vermelho maiores que 5. Além disso, a medição da razão poeira-metais em galáxias ao longo de um grande intervalo de tempo cósmico é surpreendemente constante, o que contrasta com a evolução da formação estelar. É, portanto, necessário um mecanismo extra para a produção de poeira. Foi proposto que o crescimento de grãos de poeira no meio interestelar seja a fonte de poeira que se encontra em falta, tanto no Universo local como no passado.

Um grão de poeira irá equilibrar a uma temperatura que é dependente da intensidade do seu campo de radiação local, e também é dependente das propriedades óticas do grão. O aquecimento de grãos de poeira é efetuado, principalmente, por absorção de luz estelar, contudo, radiação do disco de acreção em torno de um buraco-negro super-massivo num Núcleo Galático Ativo é, também, um importante mecanismo para o aquecimento de poeira. A emissão de galáxias no

infravermelho é geralmente atribuída a três componentes de poeira interestelar. A comprimentos de onda do infravermelho longínquo, a emissão de galáxias é principalmente dominada por grãos de poeira em equilíbro térmico a baixas temperaturas. O espectro no infravermelho médio é dominado por bandas de emissão fortes características a diversos comprimentos de onda. É geralmente aceite que os responsáveis por tal são transições vibracionais de moléculas de Hidrocarbonetos Aromáticos Policíclicos. O espectro no infravermelho médio também inclui uma componente de emissão contínua, atribuída a uma distribuição contínua de grãos de poeira pequenos com capacidade calorífica muito baixa. Esta visão deriva de modelos com os tamanhos e propriedades óticas de grãos de poeira e de Hidrocarbonetos Aromáticos Policíclicos no meio interestelar da Via Láctea e de galáxias próximas.

Ao estudar a poeira e a sua evolução, grande parte dos estudos baseam as suas suposições nos comprimentos de onda no infravermelho longínquo, uma vez que é nesses comprimentos de onda onde a maioria da energia reside, enquanto que a energia a comprimentos de onda menores é estimada através de relações empíricas locais, ou é mesmo desprezada. No entanto, estes regimes espectrais podem ter importância nas regiões mais próximas de fontes de aquecimento e, portanto, podem não evoluir da mesma forma que a poeira que radia no infravermelho longínquo, o que significa que os modelos utilizados atualmente podem ser inapropriados para estudar a poeira como um todo nas galáxias.

O estudo nesta dissertação é uma continuação do trabalho apresentado em Messias et al. (2013), onde dados no infravermelho próximo foram utilizados para estudar a evolução de poeira quente a comprimentos de onda específicos. Este estudo visa confirmar um resultado obtido em Messias et al. (2013), onde se depararam com uma clara diferença na evolução da densidade de luminosidade entre os comprimentos de onda no infravermelho próximo estudados e os comprimentos de onda no infravermelho longínquo retirados da literatura. O objetivo é verificar se este resultado é de facto devido a uma evolução diferencial de poeira quente e fria, ou apenas um efeito de variação cósmica, devido à utilização de apenas um campo no céu. Para tal, o campo COSMOS (*Cosmological Evolution Survey*, com uma área de $1,8$ graus quadrados) considerado no trabalho original é novamente

utilizado. Em especial, usaram-se dados da *Infrared Array Camera* a bordo do Telescópio Espacial *Spitzer* e do *Photoconductor Array Camera and Spectrometer* e do *Spectral and Photometric Imaging Receiver*, ambos a bordo do Observatório Espacial *Herschel*. O estudo utilizou quatro intervalos de desvio para o vermelho (ou distância), com idades do Universo compreendidas entre 3.455 Giga anos e 12.788 Giga anos, e cinco tipos espectrais diferentes de galáxias, com mais de 83 mil fontes, no total.

Considerando que o telescópio *Herschel* não possibilita a detecção de grande parte das galáxias detetadas pelo *Spitzer*, é necessário um método alternativo de as estudar no infravermelho longínquo. Este consiste em "recortar" pedaços de imagem centrados nas posições das galáxias em estudo, e "empilhá-los". Ao fazê-lo, o ruído circundante irá reduzir até um valor onde a média ou a mediana do fluxo da população encontra-se mais elevada que o nível de ruído, obtendo, assim, uma detecção. Este método é utilizado ao longo deste trabalho. Porções de imagens de 41 por 41 píxeis foram cortadas em torno de cada galáxia da população de interesse. Foram, posteriormente, estimadas as medianas ponderadas a cada posição dos píxeis. O fluxo total calculado em cada pilha foi obtido utilizando um ajuste Gaussiano.

O primeiro passo foi caracterizar a amostra em tipos espectrais e distâncias para avaliar a sua evolução. Para tal, a amostra foi separada em populações e em intervalos de desvios para o vermelho tendo sido então empilhadas a cada comprimento de onda coberto pelo *Herschel*, seguido finalmente pela sua análise. Com a obtenção dos fluxos, um ajuste de corpo negro modificado para o espectro de distribuição de energia no infravermelho longínquo de cada população foi estimado. Este ajuste fornece estimativas para o fluxo (e consequente luminosidade) e temperatura. A temperatura foi utilizada para melhor compreender se os resultados da luminosidade são de facto físicos, ou um efeito de amostra incompleta, ou seja, uma fração significativa de cada população não será detetada com o aumento do desvio para o vermelho (este efeito é conhecido como o enviesamento de Malmquist). A última hipótese revelou-se o caso e, como tal, para superar este problema, as funções de densidade de luminosidade foram obtidas para cada população. Estas funções são uma ferramenta para caracterizar uma população

e como esta se distribui em magnitude. Para construir estas funções, a amostra foi então subdividida em intervalos de magnitude absoluta (ou luminosidade), e a pilha e análise de corpo negro modificado foram novamente empregues. Para superar o efeito de amostra incompleta, as curvas de luminosidade em relação com o desvio para o vermelho foram tomadas como funções de Schechter, possibilitando o completar da distribuição nos intervalos de luminosidade em falta, implicando que uma estimativa da densidade de luminosidade nas populações de galáxias mais fracas é possível. Integrando o melhor ajuste da função de Schechter fornece a densidade de luminosidade de cada população a cada desvio para o vermelho. Os resultados aqui obtidos não corroboram os resultados esperados, o que implica que desvios para o vermelho mais baixos são altamente afetados por variação cósmica, provocando a evolução diferencial reportada em Messias et al. (2013). No entanto, concluiu-se que a relação entre densidades de luminosidade do infravermelho longínquo e do infravermelho próximo correlacionam-se bem com magnitude. Finalmente, galáxias de tipo elíptica e aquelas que mostram atividade nuclear obscurecida não possuem dados suficientes para que se chegue a qualquer conclusão.

Uma vez que se crê que os intervalos de desvio para o vermelho mais baixos são altamente afetados por variação cósmica, é necessária confirmação destes resultados num campo mais abrangente do céu, que fornecerá um maior número de objetos. Isto irá permitir erros estatísticos mais baixos e confirmar, ou refutar os resultados aqui obtidos. Além disso, também permitirá uma análise mais completa das galáxias de tipo elíptica e galáxias que apresentam atividade nuclear obscurecida a baixos desvios para o vermelho.

Palavras-chave: Poeira, Infravermelho, Galáxias, Evolução, Densidade de Luminosidade.

Contents

List of Figures

List of Tables

Chapter 1

Introduction

Dust is mostly comprised of Silica- and Carbon-based particles, which will emit at infrared (IR) wavelengths when heated by ultraviolet (UV) or optical light. However, at ground-level, observations taken in the IR spectral regime are plagued by atmospheric emission and absorption (Figure 1.1), preventing a direct study of dust. On the other hand, dust leaves a characteristic imprint in the spectral energy distribution (SED) of a galaxy, absorbing more shorter wavelength photons in comparison to longer wavelength ones, inducing a redder color to a galaxy SED (hence being frequently referred to as reddening). As a result, together with an instrumental bias toward the optical spectral regime, it is not unexpected that the first evidences for the existence of dust came from optical observations (Trumpler 1930). Since then, space- and ground-based technology has improved to a point where a direct assessment of dust properties is possible, but even today a significant part of our knowledge of interstellar dust is still based on studies of its attenuation of UV-to-optical light (see Draine 2003 for a review).

With a clear need for IR observations, the *Infrared Astronomical Satellite* (IRAS) was launched in 1983 (Neugebauer et al. 1984). This mission led to the first all-sky maps in the IR in four broadband channels, centered at 12, 25, 60, and 100 μm, with a spatial resolution of $\sim 5'$. Among many key results, this facility allowed to unveil astronomical objects unseen until that time, such as deeply embedded star-forming regions, and to delineate the emission mechanisms present in Active Galactic Nuclei (AGNs).

IRAS was then followed by a powerful set of other IR to sub-millimetre

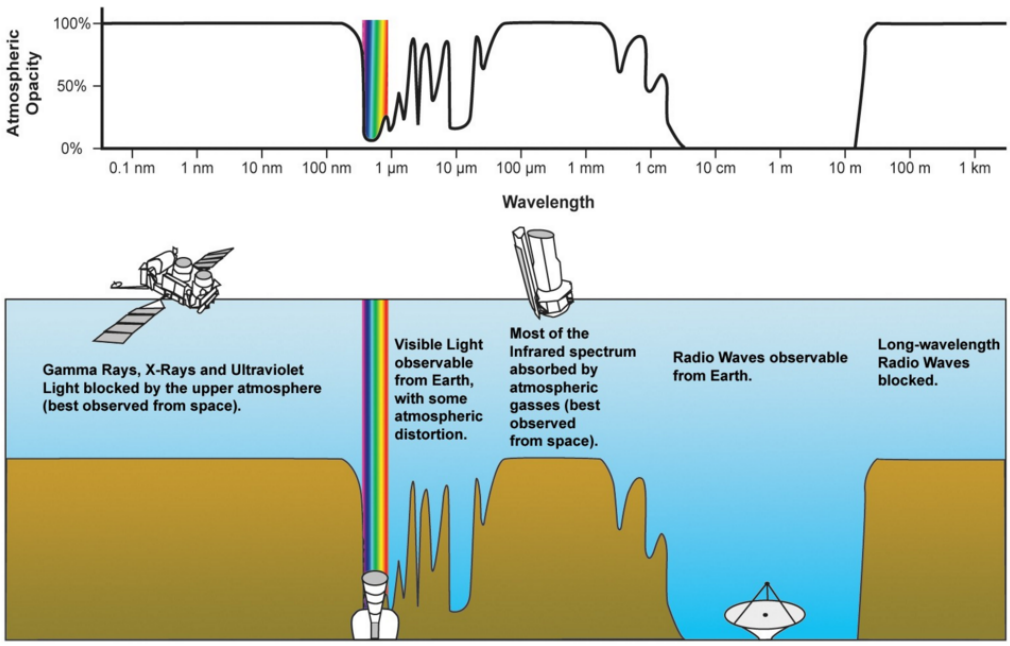

Figure 1.1: Representation of Earth's atmosphere opacity for all wavelengths. The rainbow represents the visible wavelengths. Image courtesy of NASA/JPL-Caltech.

observing facilities: NASA's *Cosmic Background Explorer* (COBE), launched in November of 1989; ESA's *Infrared Space Observatory* (ISO), launched in November of 1995; the Submillimetre Common-User Bolometer Array (SCUBA), mounted in 1997 on James Clerk Maxwell Telescope; the *Spitzer* Space Telescope, launched in August of 2003; ESA's *Herschel* Space Observatory (formerly called *Far Infrared and Sub-millimetre Telescope* or FIRST), launched in May of 2009; and NASA's *Wide-field Infrared Survey Explorer* (WISE), launched in December of 2009. This telescope armada has shown that most of the star-formation occurring in today's Universe is obscured. In fact, populations of IR-luminous galaxies at redshifts (or z) up to ~ 1.5 comprise around $70 - 80\%$ of far-IR (FIR) and 30% of sub-millimeter backgrounds, and it is likely that they dominate star-formation activity at high z (e.g. Chary & Elbaz 2001; Le Floc'h et al. 2005; Dole et al. 2006).

Dust being so prominent at high redshifts may seem unanticipated, consid-

ering that dust would be expected to be non-existent in the absence of metals. However, ISO and *Spitzer* have shown just the opposite: dust can be abundant in metal-poor environments and the IR spectra of low metallicity star-forming dwarf galaxies show a diversity of shapes (e.g. Madden et al. 2006; Wu et al. 2006). More recently, it has also been shown that significant amounts of dust can be observed quite early in the Universe (e.g. Bertoldi et al. 2003; Vieira et al. 2013; Riechers et al. 2013).

It is now known that dust plays a very important role in the astrophysics of the interstellar medium (hereafter, ISM). It is relevant in the thermodynamics and chemistry of the gas, and it is crucial to star-formation itself. This owes to the fact that dust is a molecular-gas formation-catalyst expectedly via the Langmuir–Hinshelwood or Eley–Rideal mechanisms, whereby an atom in a given surface interacts, respectively, with another one on that surface or one in the gas phase. This process is then followed by gas desorption and can dominate the gas phase chemical enrichment mechanism by more than ten orders of magnitude (Pirronello et al. 1997a,b, 1999 and references therein). On top of this, while molecules are being formed at the surface of dust, it is also being protected from the intense UV radiation field, thus being an extra help to molecular-gas self-shielding in creating the ideal conditions for star-formation to occur in molecular clouds (Krumholz et al. 2008; Krumholz 2012).

1.1 Dust Formation and Heating

It is estimated that no less than 30% of the energy emitted as starlight in the Universe is reradiated by dust in the IR (Bernstein et al. 2002), therefore, understanding the physical processes responsible for its formation throughout cosmic time has very important cosmological implications.

Dust can be formed by Asymptotic Giant Branch (AGB) stars, or Supernovae (SNe; Michałowski et al. 2010). Theoretical works have shown that an AGB star and a SN can produce, respectively, up to $\sim 4 \times 10^{-2}\ M_{\odot}$ (Morgan & Edmund 2003; Ferrarotti & Gail 2006) and $1.32\ M_{\odot}$ (Todini & Ferrara 2001; Nozawa et

al. 2003) worth of dust. However, in the case of SNe, less than $\sim 0.1\ M_{\odot}$ actually survives the shocks (Bianchi & Schneider 2007; Cherchneff & Dwek 2010; Lau et al. 2015). Based on these dust yields and the dust masses of Quasi-Stellar Objects (QSOs), Michałowski et al. (2010) showed that an extra mechanism of dust production (namely, a nonstellar one) is necessary to account for dust present in QSOs at redshifts up to 5, especially since there was little time for these objects to produce a significant amount of dust. In addition, the surprisingly constant dust-to-metals ratio measured in galaxies over a wide range of cosmic time also indicates that a rapid mechanism of dust formation is needed, requiring the dust formation timescales to be of the same order as the metal enrichment timescales (Zafar & Watson 2013).

Dust grain growth in the ISM (Draine 2009) on dust seeds produced by stars (Bianchi & Schneider 2007; Cherchneff & Dwek 2010) has been proposed as the extra source of dust needed in galaxies at both high redshifts (e.g. Michałowski et al. 2010; Valiante et al. 2011), and at low redshifts (e.g. Inoue 2011; Boyer et al. 2012), which could make up the shortfall in the dust budget of galaxies (Rowlands et al. 2013). The problem with determining the origin of the dust in galaxies and its lifecycle comes from a lack of large enough samples of sources where it is possible to study this issue.

A dust grain will equilibrate to a temperature that depends on the intensity of the radiation field where it is located, and it will also depend on its optical properties derived by its chemical composition, size, and structure (Draine & Li 2007). The heating of interstellar dust grains is done primarily by absorption of starlight (Draine 2003), but light from the accretion disk around a super-massive black-hole in an AGN is also an important source of dust heating (Nenkova et al. 2008; Hönig & Kishimoto 2010).

Observing the black body spectrum (Figure 1.2), it is discernible that cooler dust has a peak in the FIR, while at the sublimation temperature (around 1500 K; Hillenbrand et al. 1992) dust radiates with an emission peak in the near-IR (NIR). Since dust originates in stellar formation regions and is present around AGNs, it is possible to observe its emission in the NIR, but, because dust heating by UV

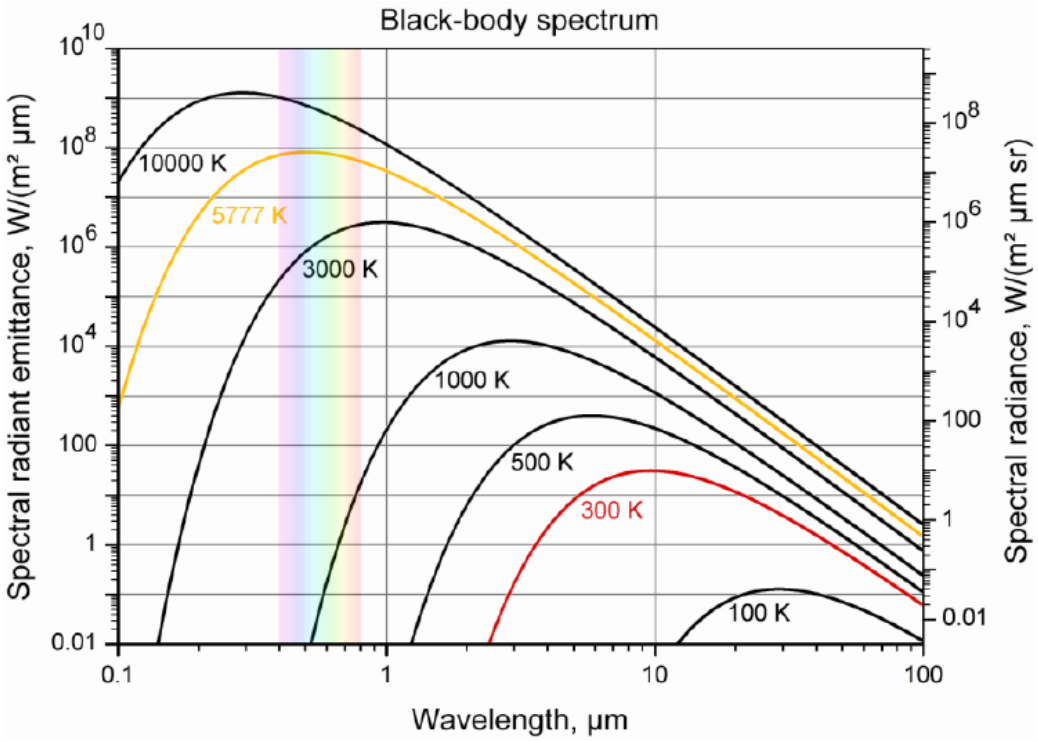

Figure 1.2: Example of black bodies at different temperatures. The rainbow represents the visible wavelengths. Image courtesy of Green, R. (January, 2010). `http://how-it-looks.blogspot.pt/2010/01/infrared-radiation-black-bodies-and.html`.

and optical photons is quantized and stochastic, the temperature of a dust grain is time dependent (Draine 2003).

1.2 Main Dust Components

The IR emission from galaxies is generally attributed to three main components of interstellar dust: "very small grains" (with sizes typically less than $0.01\ \mu m$), which are stochastically heated to high temperatures by the absorption of single UV photons; "big grains" (with sizes typically between 0.01 and $0.25\ \mu m$), which are in thermal equilibrium with the radiation field; and Polycyclic Aro-

matic Hydrocarbon (hereafter, PAHs), which produce strong emission features at wavelengths between 3 and 20 μm. This depiction derives from models of the sizes and optical properties of dust grains and PAHs in the ISM of the Milky Way and nearby galaxies (e.g. Mathis et al. 1977; Draine & Lee 1984; Leger & Puget 1984).

At FIR wavelengths (Figure 1.3), galaxy emission is mostly dominated by dust grains in thermal equilibrium at low temperatures (da Cunha et al. 2008). Their temperatures depend on the intensity of the radiation field where they are located. This is the reason why the peak of the FIR SED of a galaxy is a good indicator of dust heating in the ISM (da Cunha et al. 2008).

The mid-IR spectra of most normal star-forming galaxies are dominated by strong emission features at 3.3, 6.2, 7.7, 8.6, 11.3 and 12.7 μm (Figure 1.3), first discovered by IRAS and probed extensively by ISO's spectrometers. Although still uncertain, the carriers of these features are generally accepted to be vibrational transitions in PAH molecules (Allamandola et al. 1989, see also Tielens 2008 for a review) excited to high internal energy levels after the absorption of single UV photons (Leger & Puget 1984; Allamandola et al. 1985; Léger et al. 1989; Allamandola et al. 1999). PAH emission tends to peak in the "photodissociation regions" at the interface between ionized and molecular gas in the outskirts of HII regions, where PAH molecules can survive and transient heating is most efficient (e.g. Cesarsky 1996; Verstraete et al. 1996; Rapacioli et al. 2005). PAHs can emit as much as $\sim 10 - 20\%$ of the IR energy budget (Brandl et al. 2006; Smith et al. 2007). Through the photoelectric effect, PAHs heat the gas in the ISM (e.g. Hollenbach & Tielens 1997), reinforcing the coupling of gas and dust components. Because of their dominance in this spectral regime, PAHs have been used to identify galaxies with intense star-formation at $z \sim 2 - 3$ and to estimate their bolometric luminosities (e.g. Houck et al. 2007; Weedman & Houck 2008; Dey et al. 2008).

The mid-IR spectra of star-forming galaxies (out to wavelength ~ 40 μm) also include a component of smooth continuum emission (Figure 1.3), generally attributed to a continuous distribution of small grains with very low heat capacity,

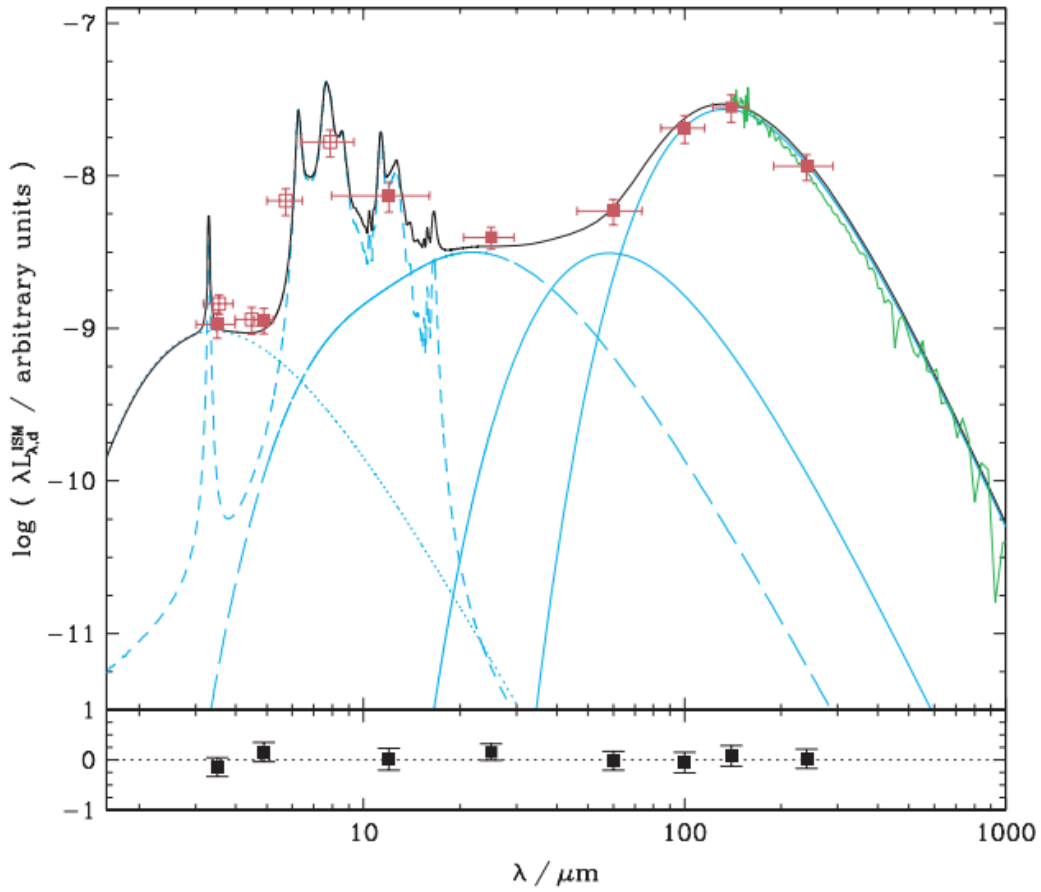

Figure 1.3: Model fit (black) to an mean SED in the IR of our Galaxy. The blue lines show the different components of the model: NIR continuum (dotted); PAHs (short-dashed); hot mid-IR continuum (long-dashed); and warm and cold grains in thermal equilibrium (solid). The squares and green line are observations performed by several teams. Image courtesy of da Cunha et al. (2008).

which are stochastically heated to transient high temperatures by the absorption of single UV photons (e.g. Sellgren 1984).

The idea of transient heating of small grains was first introduced by Greenberg (1968). However, its importance was only recognized when NIR emission of reflection nebulae was detected (Sellgren, Werner & Dinerstein 1983) and the IRAS detection of 12 and 25 μm Galactic emission, which was much higher than the

emission expected for interstellar dust at $T \approx 20$ K (Boulanger & Pérault 1988). Later, the Diffuse Infrared Background Experiment (DIRBE), an instrument on COBE, confirmed this result.

1.3 Luminosity Functions as a tool to assess Galaxy Evolution

One of the biggest problems in Astrophysics is the ability to explain and predict how galaxies distribute in luminosity, mass or any other physical property of interest. While many of these are model-dependent, a galaxy's luminosity is the most directly-derived property an observer can extract from observations. As a result, the distribution in luminosity of galaxies, known as luminosity functions, have been one of the best ways to assess galaxy evolution and test models. Recurring problems are the overestimation of the faint-end slope and the number counts of massive galaxies at any redshift. These issues are tackled with physically-motivated mechanisms which avoid gas turning into stars (such as star-formation and AGN feedback), improving our knowledge of galaxy evolution (see Henriques et al. 2015 for the latest developments).

Hubble & Humason (1931) showed early evidence of the usefulness of the luminosity function, studying galaxies of 8 clusters plus 15 isolated galaxies. One particular case, the Coma Cluster, is interesting, because, with the improvement of instrumentation, which made detection of fainter dwarf galaxies possible, it has been discovered that the shape of the Coma Cluster luminosity function's faint-end was not as previously thought (e.g. Mobasher & Trentham 1998), prompting an improvement in the theory with each new discovery regarding the Coma Cluster (see Biviano 1998 for a review).

A common approximation of a galaxy luminosity function is the Schechter function (Schechter 1975, 1976). Its expression has the form

$$\phi(L) = (\tfrac{\phi^*}{L^*})\ (\tfrac{L}{L^*})^{\alpha}\ e^{-(L/L^*)},$$

where ϕ^* is the normalization density and L the luminosity. α is the power law slope at low L, while at high L, the density drops exponentially. L^* is a character-

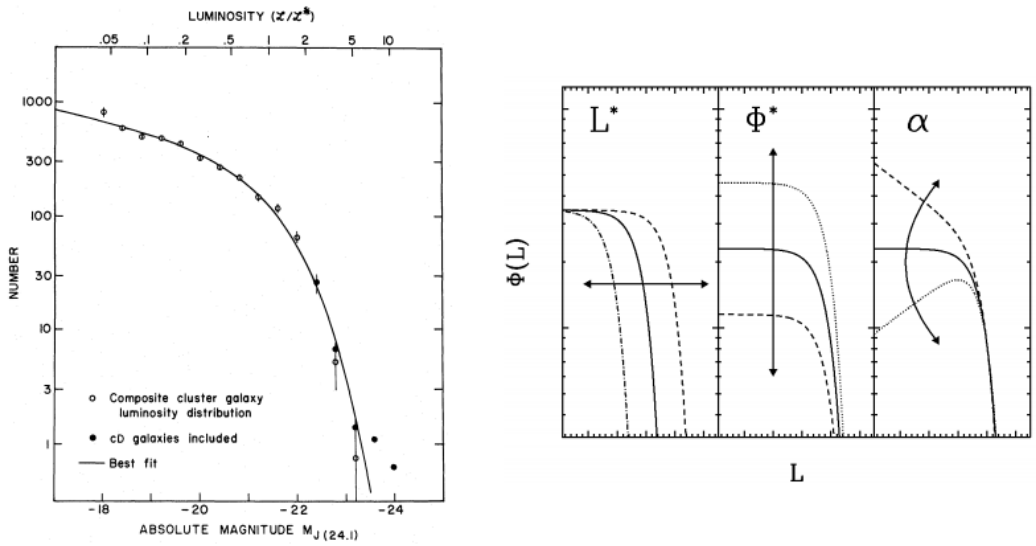

Figure 1.4: The left hand side shows an example of the Schechter function. The right hand image shows what influence each characteristic value, ϕ^*, L^*, and α, has in the shape of the curve. Images courtesy of: Left - Schechter (1975, 1976); Right - Messias (2011).

istic luminosity that separates these two regimes. Figure 1.4 shows examples of this function with an illustration of what each parameter is responsible for.

This function can be expressed in magnitudes, using the relation

$$M - M^* = -2.5\, log(\tfrac{L}{L^*}),$$

which yields

$$\phi(M) = \tfrac{ln10}{2.5}\ \phi^*\ 10^{0.4\ (\alpha+1)(M^*-M)}\ exp[-10^{0.4\ (M^*-M)}],$$

where M is the absolute magnitude and M^* is the characteristic absolute magnitude.

The total luminosity density of galaxies can also be calculated with exploitation of the Schechter function:

$$\rho_{tot} = \int_0^\infty L\ \phi(L)\ dL = L^*\ \phi^*\ \Gamma(\alpha + 2),$$

where the Gamma function $\Gamma(x)$ is defined as

$$\Gamma(x) = \int_0^\infty y^{(x-1)}\, e^{-y}\, dy$$

The luminosity density of galaxies whose luminosities exceed L is calculated the same way, only, the integral limits vary from L to ∞, and, in place of the Gamma function, the incomplete Gamma function is used:

$$\Gamma(x, s) = \int_s^\infty y^{(x-1)}\, e^{-y}\, dy$$

In some occasions, multiple Schechter functions are needed to better fit the data (e.g. Drory et al. 2009), however, one is generally enough to characterize a galaxy luminosity function.

1.4 Motivation and Goals

There is a vast number of studies on dust properties and how it influences galaxy evolution and our knowledge of it. However, since it is in the FIR that most of the energy resides, studies base their assumptions on those wavelengths, meaning they use only FIR data and infer NIR and mid-IR based on local relations (see Dale & Helou 2002) or even neglect those spectral regimes. Yet, the NIR and mid-IR spectral regimes may play a role in the regions closer to the heating sources, and might not evolve the same way as the dust radiating in the FIR, thus being inappropriate to use these models or assumptions to study dust throughout cosmic time.

The study to be presented in this dissertation is a continuation of the work shown in Messias et al. (2013), in which NIR data was used to study hot-dust evolution in specific wavelengths, namely, $3.3\ \mu m$ and $4.2\ \mu m$, to include or exclude PAH contribution, respectively.

Since the intention is to study dust alone, and there is a significant stellar contribution at 3.3 and $4.2\ \mu m$, the stellar emission must be subtracted from the galaxy's SED. To accomplish this, let us refer to Figure 1.5, where three different galaxy models, aged between 50 Myr and 13 Gyr (dotted lines), show that

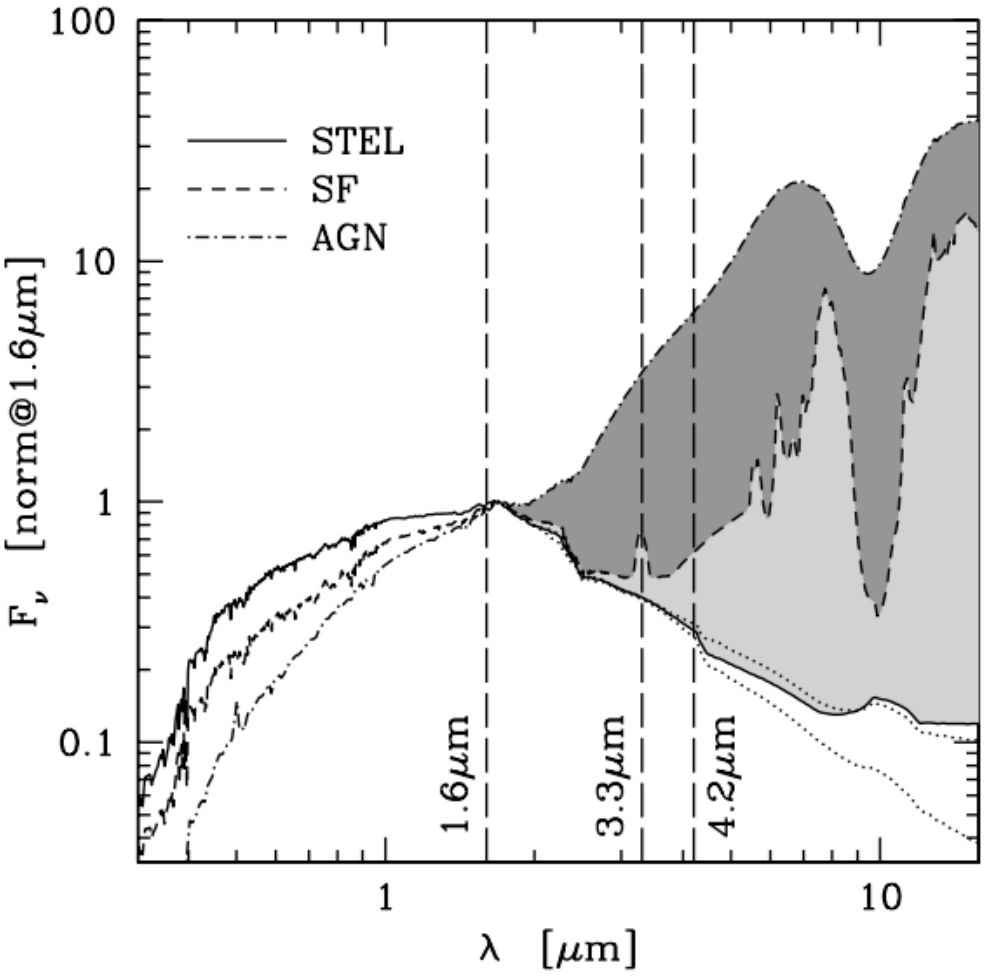

Figure 1.5: Separation of the IR emission into stellar and dust+PAH contributions. The white area below the solid lines is stellar contribution and the gray areas are contributions from stellar-heated and AGN-heated dust (light and dark gray, respectively). Image courtesy of Messias et al. (2013).

the SED of the stellar emission between 1.6 and 4.2 μm has an age-independent shape, because it is dominated by cold stars, which live longer than hotter stars. This property is key since, based on a stellar-dominated spectral region (1.6 μm or H-band), one can estimate the stellar emission at $3-4$ μm. As a result, whatever flux-excess is above that estimated stellar flux, it will be assigned to hot-dust or PAH emission.

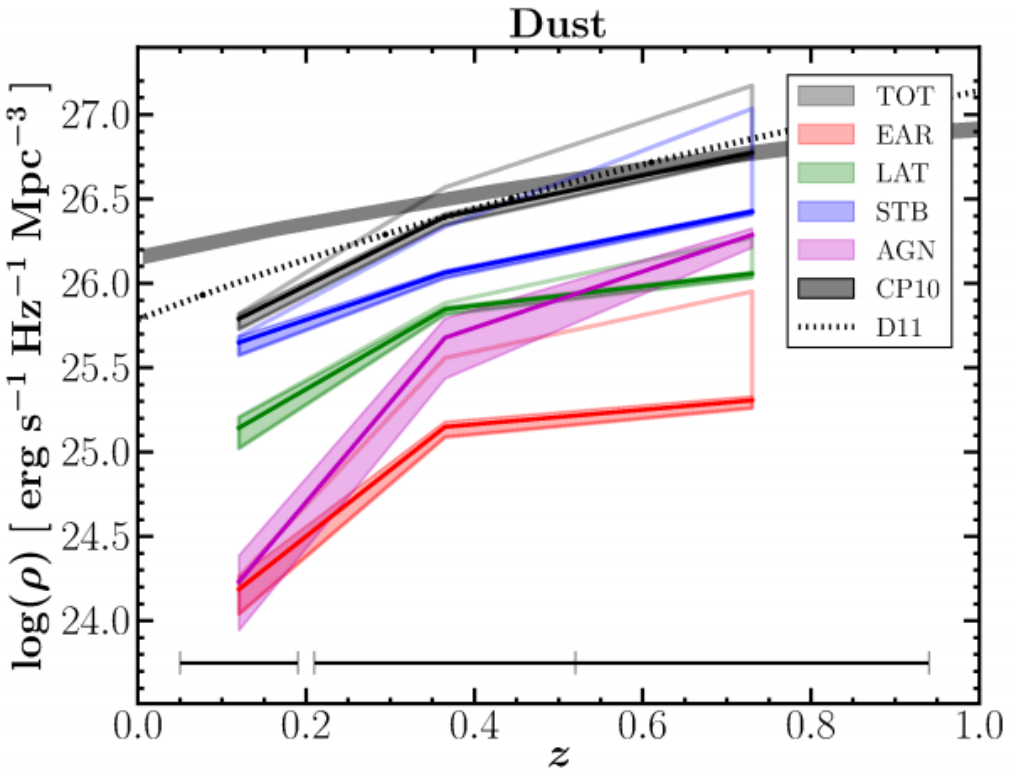

Figure 1.6: Evolution of the hot-dust luminosity density with redshift. It is shown independently for each spectral population: Total (TOT), Early Type (EAR), Late Type (LAT), STBs, and AGNs. The gray shaded region refers to the cold-dust luminosity density derived from FIR observations (Magnelli et al. 2009; Chary & Pope 2010 = CP10) and is normalized to the dust luminosity density value of the Total Population at $0.52 < z < 0.94$. Image courtesy of Messias et al. (2013).

Figure 1.6 shows the result that this dissertation aims to confirm. For the whole galaxy population there is a distinct difference in the luminosity density evolution at NIR (TOT shaded region) and FIR wavelengths (CP10 shaded region; Magnelli et al. 2009; Chary & Pope 2010). The goal of this dissertation is to verify whether this is due to a differential evolution of hot- and cold-dust, or is an effect of cosmic variance, since the original work only used one field in the sky.

Throughout this dissertation the AB magnitude system is used. A ΛCDM cosmology is assumed with $H_0 = 70\ km\ s^{-1} Mpc^{-1}$, $\Omega_M = 0.3$, and $\Omega_\Lambda = 0.7$.

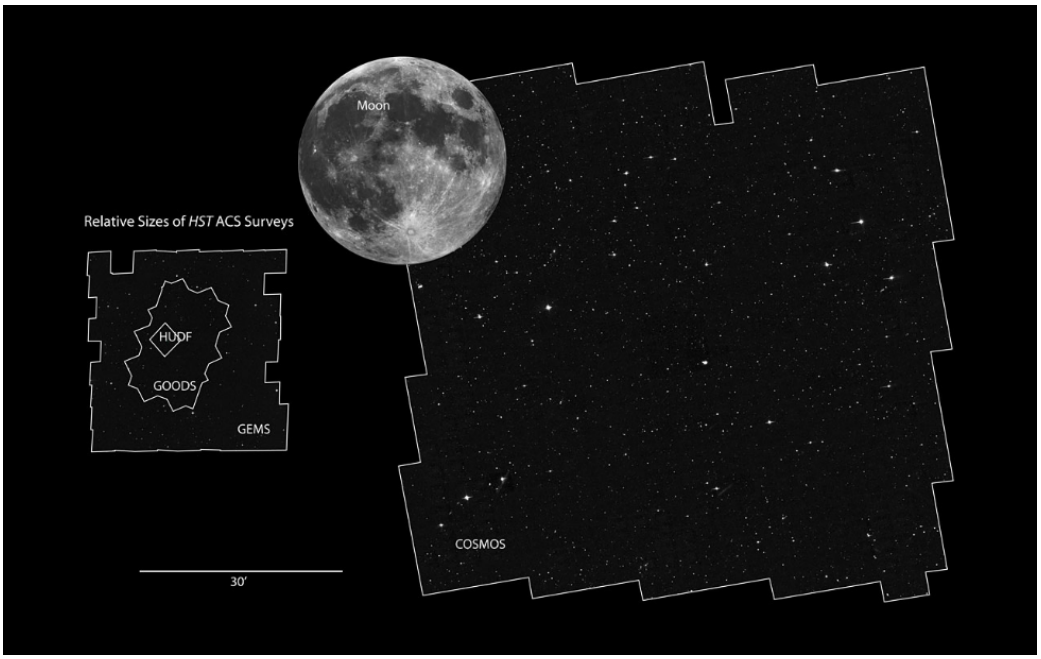

Figure 1.7: Comparison between different surveys, including COSMOS, and Moon sizes. Image courtesy of NASA, ESA and Z. Levay (STScI).

1.5 Observations

In order to compare the contribution from hot-dust at rest-frame $3.3\ \mu m$ and that of cold-dust at FIR wavelengths (from $0 < z < 0.2$ up to $0.9 < z < 1.9$) this work makes use of data retrieved from the $1.8\ deg^2$ Cosmological Evolution Survey (COSMOS; Scoville et al. 2007; Figure 1.7). Namely, this analysis is mostly dependent on data from the *Spitzer*-COSMOS survey (Sanders et al. 2007), *Herschel* Multi-tiered Extragalactic Survey (HerMES; Griffin et al. 2010; Leveson et al. 2010; Oliver et al. 2012; Viero et al. 2013a), and PACS Evolutionary Probe (PEP; Poglitsch et al. 2010; Lutz et al. 2011).

The wavelengths used are 3.6, 4.5, 5.8 and $8\ \mu m$ from the *Spitzer*-COSMOS survey, for the NIR data; 100 and $160\ \mu m$ from PEP, for the FIR data; and 250, 350 and $500\ \mu m$ from HerMES, for the FIR data.

1.6 Redshift Bins and Population Description

The distances to the observed galaxies are based either in spectroscopic estimates (Trump et al. 2009; Lilly et al. 2009; Kartaltepe et al. 2010; Brusa et al. 2010; Fu et al. 2010; Knobel et al. 2012), or, when these are not available, in the photometric template-fitting analysis pursued by Ilbert et al. (2009) and Salvato et al. (2011). Using these estimates, this study considered the following four redshift bins:

- $0.05 < z < 0.19$ (referred to as $z \sim 0.12$ henceforth), corresponding to Universe ages ranging from 12.788 Gyr to 11.136 Gyr;
- $0.21 < z < 0.52$ ($z \sim 0.37$), or ages from 10.925 Gyr to 8.281 Gyr;
- $0.52 < z < 0.94$ ($z \sim 0.73$), or ages from 8.281 Gyr to 5.993 Gyr;
- $0.97 < z < 1.86$ ($z \sim 1.42$), or ages from 5.868 Gyr to 3.455 Gyr.

The last bin was not considered in Messias et al. (2013), however, for a better and more complete analysis, was included in this work.

In each of these redshift bins, galaxies were separated into spectral populations based on the nature of the best template fit in the analysis pursued by Ilbert et al. (2009): Early Type, Late Type, and STBs. Nevertheless, whenever a given galaxy showed IR colors characteristic of AGN activity as indicated by the AGN IR-selection criterion proposed by Messias et al. (2012), that galaxy was then considered to belong in the AGN population, thus overwriting the previous classification from Ilbert et al. (2009). The Messias et al. (2012) may still miss some low-luminosity AGNs, due to a bright host galaxy or low AGN activity. As a result, and in addition to what was done in Messias et al. (2013), X-ray and spectroscopic data was used to identify this type of sources and remove them from the analysis. This guarantees that the observed hot-dust in the non-AGN population is clearly being heated by stellar sources. The number of galaxies comprising each of the five different populations considered in this study are described in Table 1.1.

Population	$z \sim 0.12$	$z \sim 0.37$	$z \sim 0.73$	$z \sim 1.42$
Total	4557	23765	32256	22568
Early Type	856 (19%)	3337 (14%)	3829 (12%)	1795 (8%)
Late Type	609 (13%)	3838 (16%)	5783 (18%)	4599 (20%)
STB	3044 (67%)	16201 (68%)	20861 (65%)	9267 (41%)
IR-selected AGN	32 (1%)	237 (1%)	1431 (4%)	6545 (29%)

Table 1.1: Description of the populations used and number of sources in each one of them at each redshift (rounded percentages of the total are in parenthesis). The X-ray and spectroscopically identified AGN which were not classified as IR-selected AGN are not presented in the table since they are not considered in the study.

1.7 Structure of the Document

This dissertation is organized as follows:

- Chapter 2 - The methods used to obtain the results are described in detail.
- Chapter 3 - The results obtained are presented and analyzed in this chapter.
- Chapter 4 - The conclusions of this dissertation and any future work needed for a follow-up on this study are explicit here.

Chapter 2

Methods used

As mentioned in Section 1.4, an analysis of hot-dust already exists. However, a one-to-one study between NIR and FIR for the same sample does not. To assure that the comparison is the best possible, the catalogs from the original study were employed, meaning that the sample used for the hot-dust analysis is the same applied for its cold-dust counterpart. This will give the best comparison to reach the goal of this work.

In this Chapter, the methods and techniques used to allow this comparison are described and explained in detail.

2.1 Stacking Analysis

This work makes use of data at FIR wavelengths from *Herschel*. However, the size of the telescope and survey integration times at these wavelengths do not provide a source-detection success as high as *Spitzer* at much shorter wavelengths. Although individual objects might not be detected, it is known that those objects do exist in that location and that they are emitting photons. Assuming that is so, if one stacks the pixelated noise-dominated regions around these source locations, the surrounding noise will decrease with the square-root of the number of the sources considered to a point where the average or median flux of the population is above the achieved reduced noise-level, thus resulting in a detection. This method is called stacking.

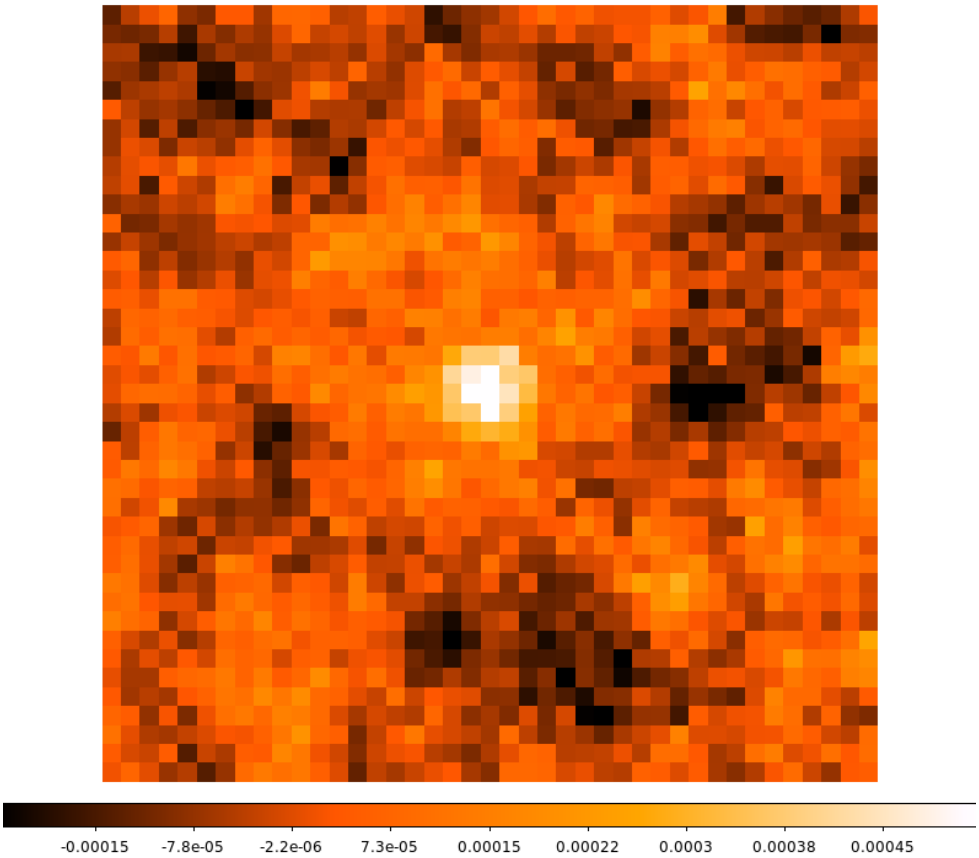

Figure 2.1: Example of the stack output, in this case, for the Total Population, at wavelength $250\ \mu m$ and $z \sim 0.12$.

In the case of the analysis pursued in this work, portions of images of 41 by 41 pixels (hereafter, stamps; see Figure 2.1 for an example) were cut around each galaxy in the population of interest (Section 1.6). These were then combined estimating the weighted median at each pixel position. The weight is used to rely more on the stamps with lower noise, and less on the stamps with a higher noise associated to them. And the median was chosen in favor of the average to prevent a bias towards too extreme fluxes.

The original background subtraction procedure in the raw data images was not sufficient for the study performed here. Given that the stacking analysis is able to achieve much deeper noise-levels, it may happen that the original background sub-

traction procedure is not accurate enough, thus resulting in non-zero background levels in the stacked images. If that is the case, a correction must be employed in order to obtain the true average and standard deviation of the background. This is performed by employing an iteration that uses the average and the standard deviation (or σ) to recalculate them several times (doing a 3σ clipping each turn), obtaining, in this manner, the best approximation possible for both variables.

Finally, in the case of a detection, the total flux of the signal is calculated for each stack using a Gaussian fit, and the total error is considered the quadrature combination of the error of the Gaussian fit and the background *rms* in each stack.

A Gaussian distribution is given by the expression

$$f(x) = a\ exp(-\tfrac{(x-b)^2}{2c^2}),$$

where a is the height of the curve's peak and b is the position of the center of the peak. c is the standard deviation, the σ of the distribution.

The standard deviation is related with the full width at half maximum (FWHM) of the Gaussian, and is given by

$$FWHM = 2\sqrt{2\ ln2}\ \sigma.$$

For this work, a two-dimensional Gaussian distribution was used, given the two-dimensional images. Its expression is

$$f(x,y) = A\ exp(-(\tfrac{(x-x_0)^2}{2\sigma_x^2} + \tfrac{(y-y_0)^2}{2\sigma_y^2})),$$

where A is the amplitude of the Gaussian, x_0 and y_0 are the center points, and σ_x and σ_y are the standard deviation in x and y, respectively. A term dependent on both x and y can be added to the expression, as well as an angle θ. However, since the aperture of the instruments is circular, there is no need for an elliptical and consequent rotation to describe the objects in this study.

A Gaussian function was considered since it explains the shape of the *Herschel* Point Spread Function (PSF; Griffin et al. 2010; Lutz et al. 2011). Also, fitting it to the final detection flux-distribution allows a better estimate of the total flux, in

comparison to an aperture-photometry procedure or relying on the peak-flux pixel (when pixel units represent beam-integrated flux).

It is worth mentioning the existence of other more complex stacking methods which aim to provide more reliable results or to tackle problems such as those resulting from clustering and beam size (Viero et al. 2013b; Mitchell-Wynne et al. 2014). In a future stage, such algorithms will be explored should we find evidences for their need, but, in this dissertation, due to computer-time saving and learning purposes, the stacking analysis described above was the one adopted throughout.

2.2 Far-infrared Properties

The first course of action was to characterize the sample into spectral types and distances to assess their evolution. To do so, the sample was separated into populations, redshift bins, and stacked at each *Herschel* band (100 to 500 μm) as described in Section 2.1.

With the fluxes and respective errors obtained, a modified black body (mbb) fit to the FIR SED for each population at each redshift bin was computed. In this work, an optically thick mbb is used:

$$S_\upsilon(\lambda_{obs}) = \Omega(1 - exp[-(\tfrac{\lambda_0(1+z)}{\lambda_{obs}})^\beta]) \times B_\upsilon(\lambda_{obs}; \tfrac{T_d}{1+z}),$$

where B_υ is the Planck function, λ_{obs} is the observer frame wavelength, λ_0 is the rest-frame wavelength where the optical depth reaches unity, Ω is the solid angle subtended by the source, and T_d is the dust temperature (Dowell et al. 2014). This model was fitted to the data using a Markov Chain Monte-Carlo approach (see Foreman-Mackey et al. 2013 for more details).

Figure 2.2 demonstrates the results of this technique (the mbb fits with the respective stamps obtained are shown in Appendix A). This mbb fit provides estimates of the peak-flux (and subsequent peak-luminosity) and the temperature, and the respective errors associated. The temperature is analyzed for more insight of whether the results for the luminosity are in fact physical, or if they are an effect

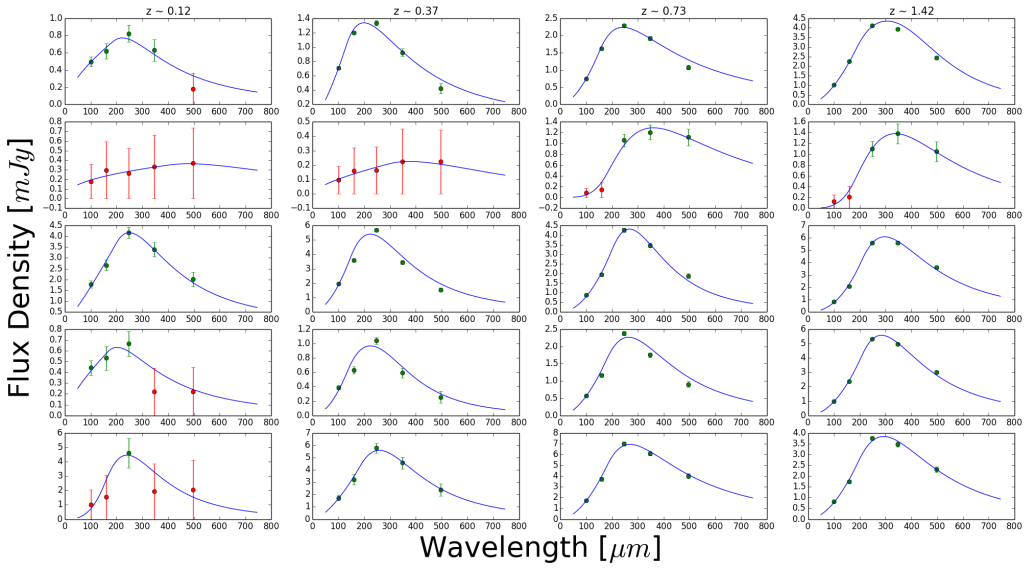

Figure 2.2: Results of the mbb fit, separating populations and redshift bins. The columns correspond to (left to right): $z \sim 0.12$, $z \sim 0.37$, $z \sim 0.73$, and $z \sim 1.42$. The rows correspond to each population (starting from the top): Total, Early Type, Late Type, STB, and AGN. The points correspond to, left to right in each plot: 100, 160, 250, 350, and 500 μm. The red points mean that the signal significance is smaller than 3σ for that stamp, and was, therefore, considered a non-detection. The green points indicate the signal significance is greater than 3σ for that stamp, and was considered a detection.

of increased sample incompleteness with increasing redshift.

Please note that, because the sample utilized in this work is extracted from a flux-limited survey, at higher redshifts, the sample is biased toward more luminous objects. Because of this, these results must be considered with care.

2.3 Luminosity Density Functions

As mentioned in the previous section, the estimated luminosity evolution inferred may be biased due to sample incompleteness. That is, at higher redshifts, less luminous objects will tend to not be detected (known as the Malmquist bias), and

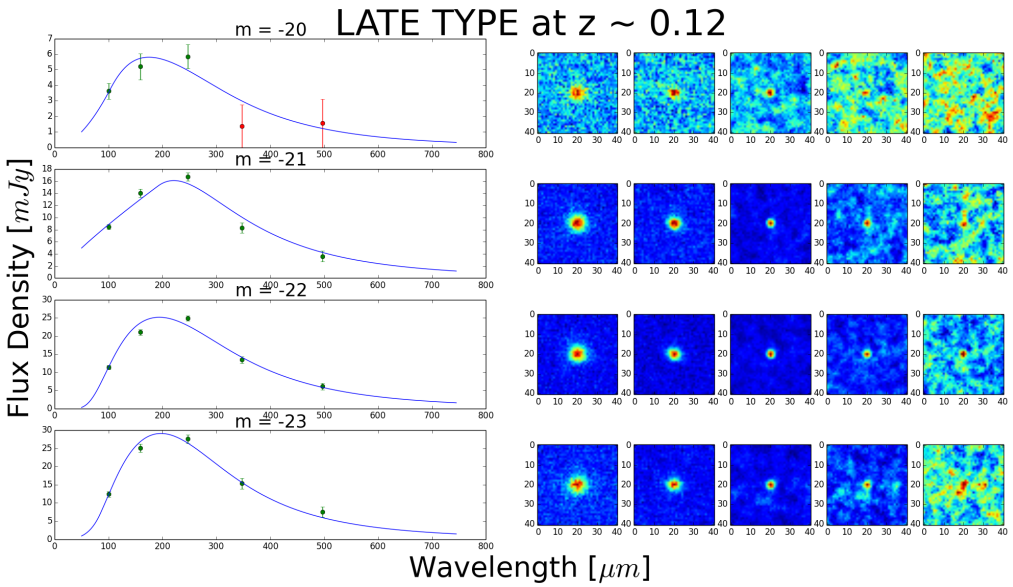

Figure 2.3: Example of the results of the mbb fit, separating populations, redshift bins, and magnitude bins, in this case, for the Late Type Population, at $z \sim 0.12$. The points correspond to, left to right in each plot: 100, 160, 250, 350, and 500 μm. The red points mean that the signal significance is smaller than 3σ for that stamp, and was, therefore, considered a non-detection. The green points indicate the signal significance is greater than 3σ for that stamp, and was considered a detection. The images are the stack results, and correspond to each point, from left to right.

the sample statistics will be dominated by the most luminous objects.

To overcome this problem, the Luminosity Density Functions (LDFs) were obtained. To build these functions, the samples were also divided into H-band absolute magnitude (luminosity) bins, and again stacked at each *Herschel* band allowing a mbb fit at each luminosity bin (see Figure 2.3 for an example; all the mbb fits with the respective stamps obtained are shown in Appendix B). The outcome of this analysis is shown in Figure 2.4 and in Figure 2.5, where the effects of sample incompleteness are apparent, with the faint-end having less information with increasing redshift.

In Messias et al. (2013) the incompleteness at the faint-end of the LDFs was

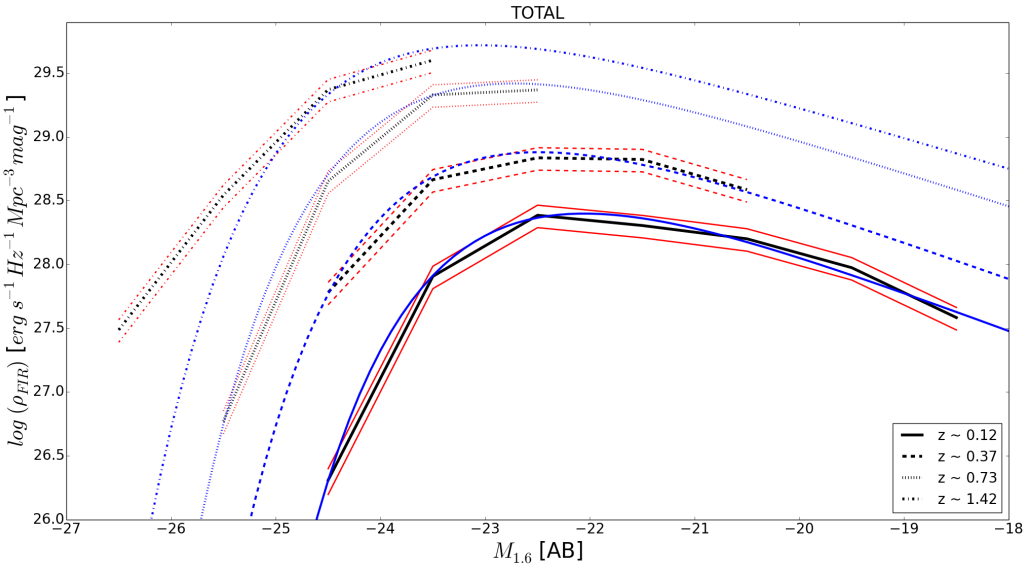

Figure 2.4: Luminosity Density versus Magnitude, with the respective Schechter function, for the Total Population. The black lines represent the points obtained with the stacking method, and the red lines are its upper and lower errors. The blue lines are the Schechter function for each curve.

corrected assuming the slope of the faint-end did not vary significantly with redshift. This is assumed once again in this analysis based on the behavior of the LDFs of the Late Type and STB populations. As a result, the shape of the lower redshift samples was used to complete the LDFs of the higher redshift samples. This exercise was not pursued for the Early Type nor the AGN populations due to the lack of data points and inconsistent LDF shapes. Consequently, these populations will not be corrected for incompleteness and will provide only luminosity density upper-limits (see Section 3.3).

The more complete LDFs of the Total, Late Type, and STB populations where then fitted with a Schechter function to obtain the characteristic values for each curve (see Section 3.3). This allows one to estimate the luminosity density of fainter galaxy samples down to $M_H = -16$ (the faintest limit considered in Messias et al. 2013) and assess the evolution with cosmic time of the samples as a whole. A bootstrapping analysis was then used to calculate the errors of each characteristic value for each Schechter function. The curves and respective Schechter

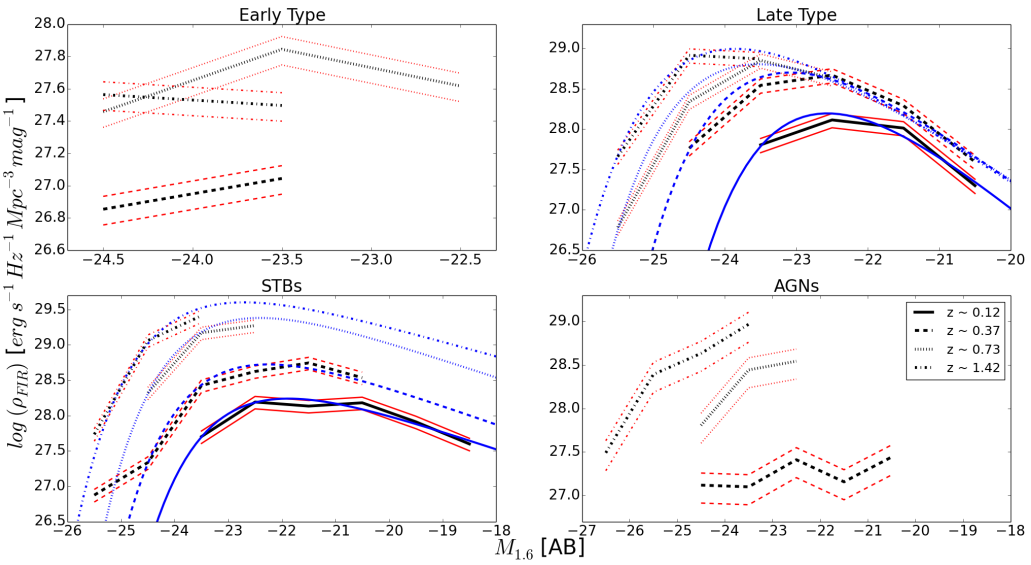

Figure 2.5: Luminosity Density versus Magnitude, with the respective Schechter function, for the remaining populations. The black lines represent the points obtained with the stacking method, and the red lines are its upper and lower errors. The blue lines are the Schechter function for each curve.

functions are represented in Figures 2.4 and 2.5. The notable discrepancy between the observed luminosity density and that predicted by a Schechter function at the bright-end (for example, the Total Population at $z \sim 1.42$) is addressed in Section 3.2.

Integrating the best fit Schechter function over the full luminosity range of interest ($M_H < -16$), one obtains the overall luminosity density and its errors of a given population, with the fainter (undetected) galaxies taken into account. Finally, the luminosity density at FIR wavelengths is compared with its counterpart at NIR wavelengths (see Section 3.3).

Chapter 3

Results

3.1 Evidences for Incompleteness Bias

From the analysis described in Section 2.2, one can infer the average cold-dust luminosity of our sample and compared with that of the hot-dust traced in Messias et al. (2013). Figure 3.1 shows such a comparison, where one can observe an increase of the cold- to hot-dust luminosity ratio with redshift in our sample, except for the Early-Type Population where there is a lack of data to conclude anything. This slight increase could be a physical result, meaning that hot-dust does evolve differently from cold-dust, or it could be an effect of incompleteness since, due to the Malmquist bias, at higher redshifts, only the more luminous objects are detected.

An evidence for incompleteness can be obtained from how the estimated temperatures of each population evolve with redshift. This is shown in Figure 3.2.

In this Figure, one can observe an escalation in the temperature with increasing redshift. Since there was no detections at low redshift for the Early Type Population, there are no points shown at $z \sim 0.12$ and $z \sim 0.37$. Even without these points, the Early Type Population still shows an increasing trend in the temperature. Once again, this increase can be a physical result, since the Universe is more active at higher redshifts, or it can be an effect of incompleteness, considering that, at higher redshifts, as mentioned before, only the more luminous objects are detected by our instruments, meaning that they are likely hotter as well. This

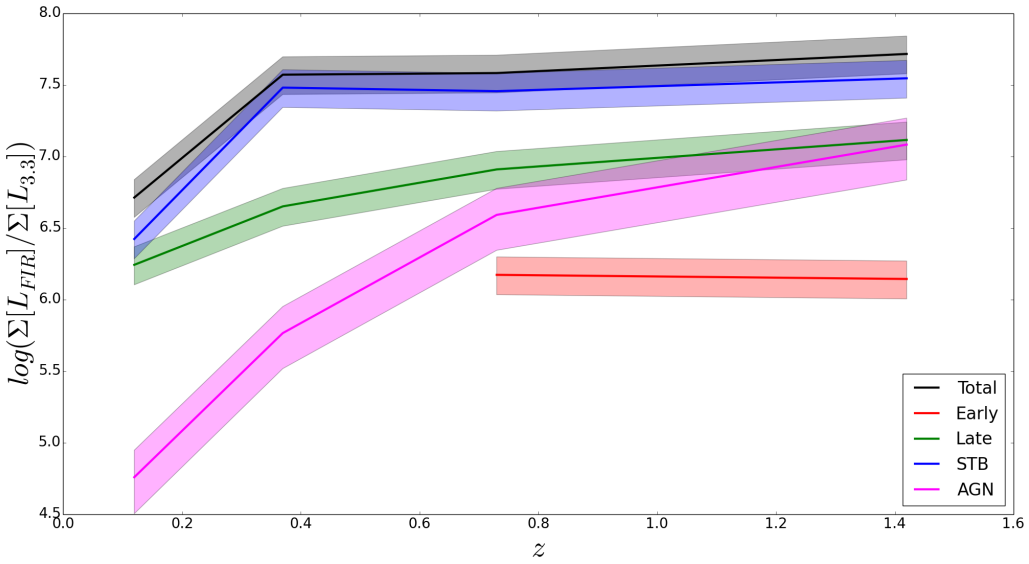

Figure 3.1: Evolution with redshift of the ratio between the total FIR and total NIR luminosities. The color coding is: black for the Total Population, red for the Early Type Population, green for the Late Type Population, blue for the STB Population, and magenta for the AGN Population. The shaded areas represent the associated errors for each population.

implies that a method must be employed in order to overcome incompleteness.

3.2 Cold-dust Luminosity Density Functions

As mentioned in Section 2.3, LDFs are a great tool to characterize a given galaxy sample, enabling one to trace its evolution across cosmic time and compare it with other samples. It can also be used as a means to correct for incompleteness and infer the integrated luminosity density, as it has been used in this work. Nevertheless, an a priori function has to be assumed - in this case, a Schechter function - which may not always properly fit the observed data-points. This was observed in the LDFs of the Total Population at $z \sim 1.42$ and of the STB Population at $z \sim 0.37$ (Figures 2.4 and 2.5). While the latter case is clearly induced by an outlier at the bright-end, the deviations observed in the Total Population at

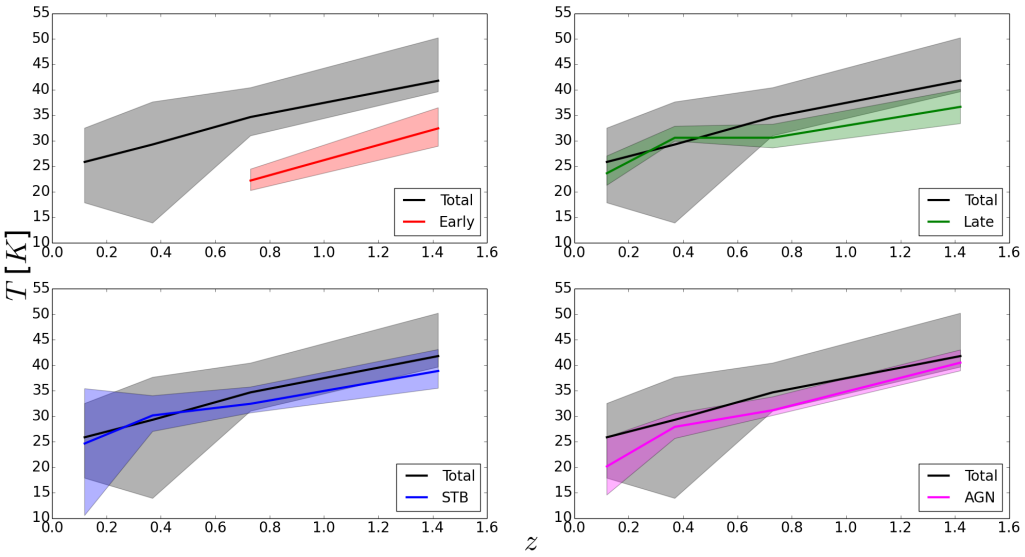

Figure 3.2: Temperature as a function of redshift for each population. In each panel each sub-sample is compared with the total one. The color coding is: black for the Total Population, red for the Early Type Population, green for the Late Type Population, blue for the STB Population, and magenta for the AGN Population. The shaded areas represent the associated errors for each population.

$z \sim 1.42$ are considered to be real. In these cases with significant deviations from a Schechter function, the outlier or bright-end data-points were not considered in the fit, but the excess implied by them was later included in the integrated luminosity density.

The main driver for these deviations at $z \sim 1.42$ may be hot-dust, around thermally pulsing AGB stars or AGNs, at temperatures close to that of sublimation or scattered AGN light boosting H-band fluxes, and, consequently, shifting some galaxies to the bright-end. This is more likely to happen in the AGN case, and Figure 3.3 corroborates such reasoning, showing that it is the AGN Population to dominate at the bright-end. But, in addition, the AGN dust torus emission may be dominating at the observed FIR wavelengths, again boosting the emission over the one expected for star-formation activity alone. At $z \sim 1.42$, the $100 - 500\ \mu m$ *Herschel* spectral range is probing the rest-frame $40 - 200\ \mu m$, and it is known

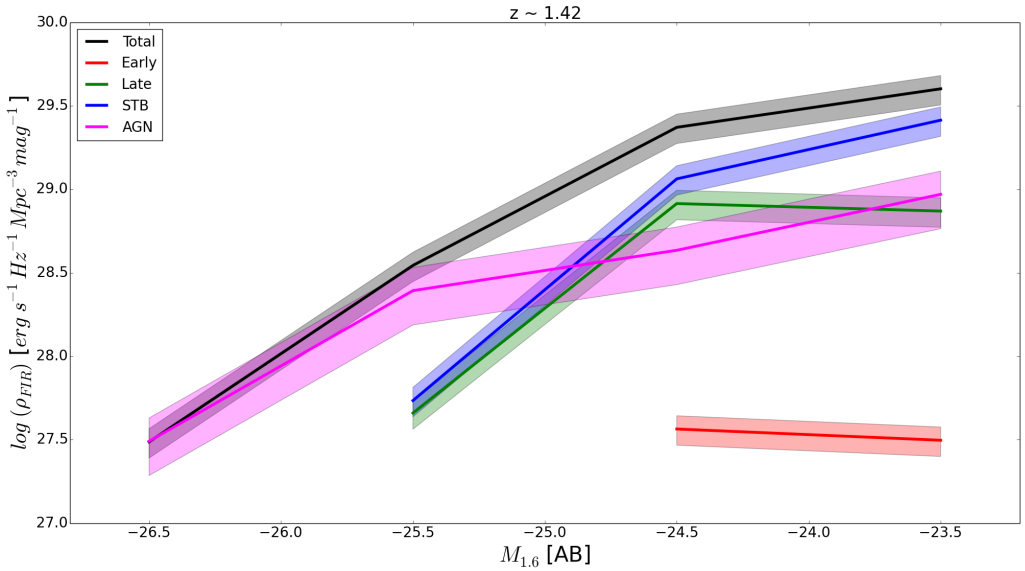

Figure 3.3: FIR luminosity density versus H-band magnitude bin, at $z \sim 1.42$. The color coding is: black for the Total Population, red for the Early Type Population, green for the Late Type Population, blue for the STB Population, and magenta for the AGN Population. The shaded areas represent the associated errors for each population.

that AGN-heated dust emission can dominate the SED of a galaxy up to $60\ \mu m$ (or even more in very rare extreme cases, e.g., Lonsdale et al. 2015), thus explaining the deviation from a Schechter-like function observed in Figure 2.4. Such behavior has also been observed in other wavelengths (Messias et al. 2013 and references therein).

The LDF best fit Schechter parameters (and corresponding errors) are listed in Table 3.1. Again, the Early Type and AGN populations were not fitted due to the lack of data points and inconsistent LDF shapes across redshift intervals. While the α parameter does not show evolution due to the assumption made to complete the LDFs to fainter magnitudes (Section 2.3), the ϕ^* and M^* parameters do show a significant evolution (as already expected from Figures 2.4 and 2.5): ϕ^* evolves with $(1+z)^{3.9}$ while M^* evolves with $(1+z)^{-1.6}$ for the Total Population, ϕ^* evolves with $(1+z)^{2.4}$ while M^* evolves with $(1+z)^{-2.0}$ for the Late Type Population, and ϕ^* evolves with $(1+z)^{4.1}$ while M^* evolves with $(1+z)^{-1.3}$ for the

Population	z	ϕ^*	M_H^*	α	LD_{FIR}	LD_{NIR}
Total	0.12	$7.18 \pm 1.54 \times 10^{28}$	-21.84 ± 0.09	-0.23 ± 0.10	$30.39^{0.56}_{0.32}$	$26.12^{0.02}_{0.05}$
Total	0.37	$2.15 \pm 0.20 \times 10^{29}$	-22.33 ± 0.06	-0.27 ± 0.05	$30.87^{0.50}_{0.37}$	$26.59^{0.03}_{0.05}$
Total	0.73	$7.24 \pm 0.77 \times 10^{29}$	-22.68 ± 0.04	-0.34 ± 0.04	$31.44^{0.49}_{0.38}$	$26.95^{0.02}_{0.03}$
Total	1.42	$1.41 \pm 0.23 \times 10^{30}$	-23.09 ± 0.02	-0.39 ± 0.08	$31.72^{0.54}_{0.34}$	$27.18^{0.02}_{0.03}$
Early Type	0.12	-	-	-	-	$25.01^{0.05}_{0.10}$
Early Type	0.37	-	-	-	-	$25.55^{0.04}_{0.08}$
Early Type	0.73	-	-	-	-	$25.68^{0.03}_{0.05}$
Early Type	1.42	-	-	-	-	$25.36^{0.03}_{0.05}$
Late Type	0.12	$3.44 \pm 0.82 \times 10^{28}$	-21.39 ± 0.40	0.86 ± 0.61	$29.55^{1.03}_{0.16}$	$25.58^{0.05}_{0.09}$
Late Type	0.37	$1.26 \pm 0.21 \times 10^{29}$	-22.06 ± 0.17	0.63 ± 0.27	$30.25^{0.70}_{0.25}$	$26.03^{0.03}_{0.05}$
Late Type	0.73	$1.73 \pm 0.24 \times 10^{29}$	-22.64 ± 0.07	0.44 ± 0.13	$30.49^{0.56}_{0.33}$	$26.13^{0.02}_{0.04}$
Late Type	1.42	$2.63 \pm 0.31 \times 10^{29}$	-22.92 ± 0.08	0.48 ± 0.11	$30.64^{0.54}_{0.34}$	$26.26^{0.02}_{0.03}$
STB	0.12	$4.75 \pm 1.09 \times 10^{28}$	-21.87 ± 0.26	-0.36 ± 0.14	$30.24^{0.62}_{0.28}$	$25.89^{0.03}_{0.06}$
STB	0.37	$1.47 \pm 0.17 \times 10^{29}$	-22.20 ± 0.07	-0.33 ± 0.06	$30.73^{0.52}_{0.36}$	$26.30^{0.03}_{0.05}$
STB	0.73	$6.57 \pm 1.05 \times 10^{29}$	-22.41 ± 0.10	-0.37 ± 0.07	$31.39^{0.52}_{0.35}$	$26.83^{0.02}_{0.03}$
STB	1.42	$1.03 \pm 0.23 \times 10^{30}$	-22.90 ± 0.22	-0.47 ± 0.10	$31.62^{0.58}_{0.31}$	$27.03^{0.02}_{0.03}$
AGN	0.12	-	-	-	-	$24.22^{0.15}_{0.27}$
AGN	0.37	-	-	-	$28.15^{0.19}_{0.25}$	$25.53^{0.28}_{0.47}$
AGN	0.73	-	-	-	-	$26.22^{0.10}_{0.17}$
AGN	1.42	-	-	-	-	$26.70^{0.07}_{0.11}$

Table 3.1: Schechter function's best fit parameter values are presented here along with the resulting integrated luminosity density for FIR and NIR wavelengths presented in a logarithmic scale. The latter are the values obtained in Messias et al. (2013). The luminosity densities are in $erg\ s^{-1}Hz^{-1}Mpc^{-3}$ units, and ϕ^* are in $erg\ s^{-1}Hz^{-1}Mpc^{-3}mag^{-1}$ units.

STB Population. Note how ϕ^* increases from $z \sim 0.12$ to $z \sim 1.42$ by factors of 20 ± 5, 8 ± 2, and 22 ± 7, respectively, for the Total, Late, and STB populations. The evolution of M^* also shows that the typical FIR emitter at $z \sim 1.42$ in same galaxy populations is brighter, respectively, by factors of 3.2 ± 0.3, 4.1 ± 1.5, and 2.6 ± 0.8 than its counterpart at $z \sim 0.12$. Note that the value for the Total Population is a lower limit since the brightest bins were not considered in the Schechter fit.

3.3 Evolution of the Far-infrared-Near-infrared Luminosity Density Ratio

From Section 3.1, it is clear that incompleteness is affecting the analysis and must be corrected. Such a correction is pursued via an analysis of the LDFs of each population, as described in Section 2.3 and presented in Section 3.2. This allows a proper luminosity density comparison with the NIR spectral regime as listed in Table 3.1.

However, before proceeding to discuss overall FIR-to-NIR luminosity density ratios, it is useful to understand how it varies with H-band luminosity. This is shown in Figures 3.4 and 3.5, where the LDFs from Section 3.2 and those at rest-frame $3.3\ \mu m$ (following the procedure from Messias et al. 2013) are compared directly via a ratio between them at each H-band luminosity bin. In Figure 3.4, one does not see a large variation of the FIR-NIR luminosity density ratio with magnitude, except at the bright-end. This trend is due to a combination of different populations behaving differently with H-band luminosity. This is evident in Figure 3.5, where the non-AGN populations show an increasing FIR-to-NIR luminosity density ratio with H-band luminosity at all redshifts, while the opposite happens for the AGN Population. Since the latter dominates the bright-end of the total population at $z \sim 1.42$, it is now understandable the break observed at the bright-end in Figure 3.4.

The decrease of the FIR-to-NIR luminosity density ratio with H-band luminosity can simply be understood as a more dominant dust-torus component in the

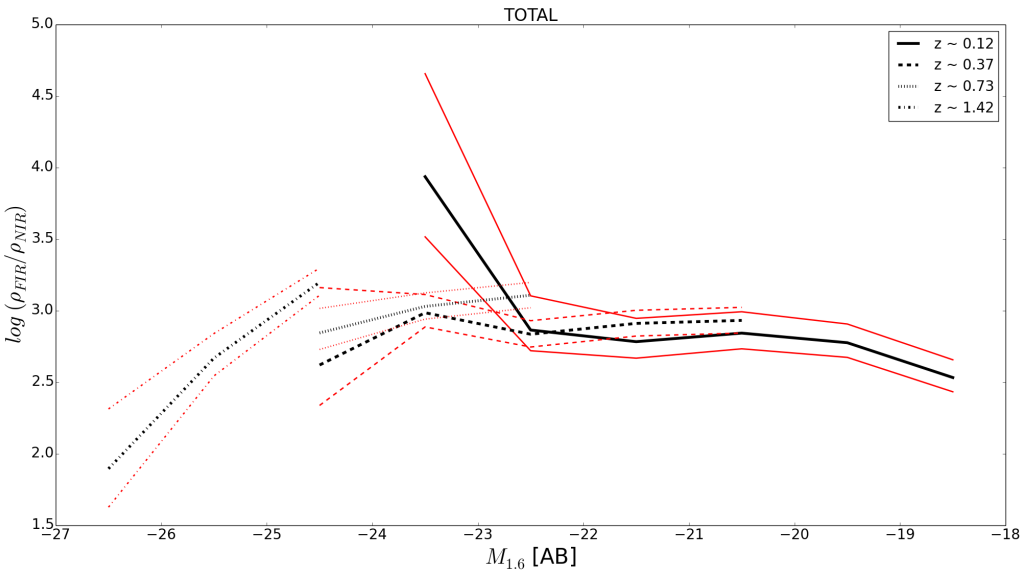

Figure 3.4: FIR-NIR Luminosity Density ratio versus Magnitude, for the Total Population. The black lines represent the ratio between the points obtained with the stacking method and the NIR points obtained in Messias et al. (2013), and the red lines are its upper and lower errors.

near- to mid-IR spectral regime in the most luminous AGN. However, the increase observed in the non-AGN populations requires a more detailed study in the future. At this stage, a possible explanation may be a higher photon budget in the most massive sources (luminous in H-band) which is still able to heat the dust in the ISM, while in lighter galaxies (fainter in H-band) there is a higher fraction of the photon budget being absorbed by the dust in the stellar neighborhood. In addition, as galaxies evolve to a more passive stage, evolved stars can also heat up the dust in the ISM giving an extra boost. Since the most massive galaxies are the ones which tendentiously reach this evolved stage quicker, one should see this effect at the bright-end, something similar to what is observed in the Late Type Population where differences at the bright-end are more noticeable.

The evolution of FIR-to-NIR luminosity density ratio with cosmic time (corrected for incompleteness) is shown in Figure 3.6, while the FIR and NIR luminosity densities values are listed independently for each population at each redshift in Table 3.1. It is clear that the analysis pursued in this work reveals no evolution

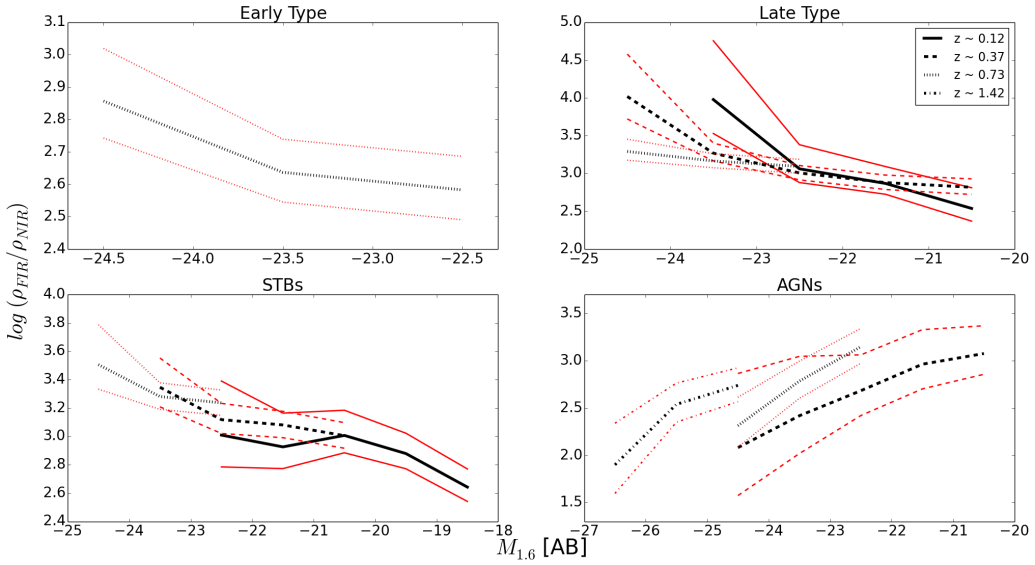

Figure 3.5: FIR-NIR Luminosity Density ratio versus Magnitude, for the remaining populations. The black lines represent the ratio between the points obtained with the stacking method and the NIR points obtained in Messias et al. (2013), and the red lines are its upper and lower errors.

as opposed to what has been proposed in Messias et al. (2013). As a result, one is led to infer that the lowest redshift bins, which provide smaller cosmological volumes, are highly affected by cosmic variance, which induced the mismatch reported in Messias et al. (2013).

The Early Type Population only has estimated limits given the failure to obtain LDFs as a result of the lack of stacked detections. Therefore, nothing can be concluded for this population. Finally, the observed evolution for the AGN Population at lower redshifts is very dependent on the selection of AGNs based on aperture photometry (which is increasingly limited to the galaxy center) implying a selection of less luminous AGNs at low redshift, and are, therefore, a distinct population from the population observed at higher redshifts. If this is the case, then a more careful analysis should be pursued for the AGN Population.

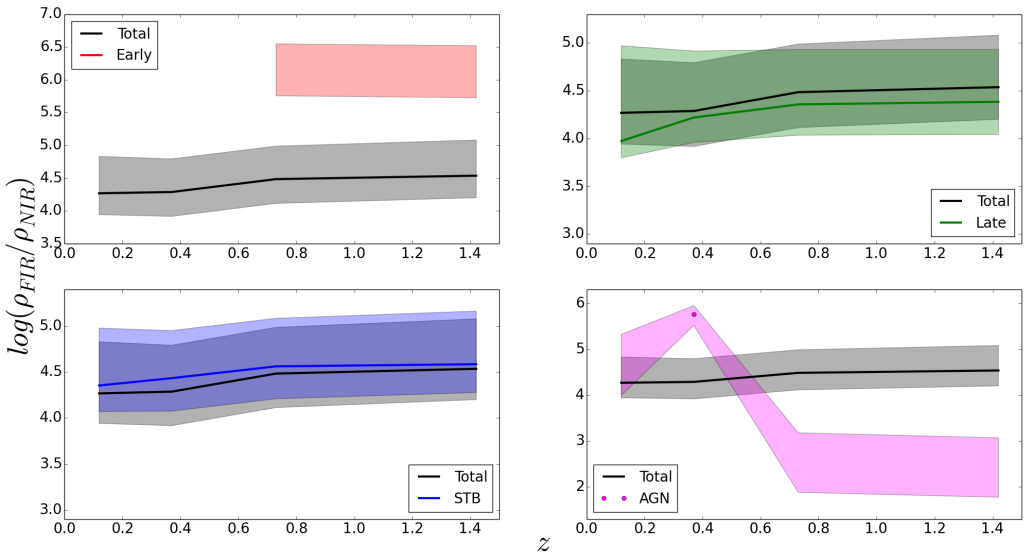

Figure 3.6: Relation between FIR and NIR luminosity densities associated with redshift divided for each population to better observe the comparison with the values obtained for the Total Population. The color coding is: black for the Total Population, red for the Early Type Population, green for the Late Type Population, blue for the STB Population, and magenta for the AGN Population. The shaded areas represent the associated errors for each population.

Chapter 4

Conclusions

In this dissertation, the evolution with cosmic time of the NIR-to-FIR luminosity density ratio was assessed in the $1.8\ deg^2$ of the COSMOS field, enabling a direct comparison of the two spectral regimes from ~ 10 Gyr ago to present-time. While *Spitzer* data (3 - 8 μm) was used to trace hot-dust, *Herschel* data (100 - 500 μm) was used to trace cold-dust in this cosmic time range.

Using a combination of stacking with mbb fitting analysis, FIR properties of different spectral populations were retrieved. The results showed evidences of incompleteness, and, therefore, a method was employed in order to overcome this issue. For this purpose, LDFs were obtained for each population. These were then fitted with a Schechter function in order to parameterize the LDFs and assess the luminosity density of the galaxy population which is fainter than the completeness limit of the survey. At higher redshift, the LDFs were empirically completed under the assumption that the shape of the LDFs at the fainter limits do not vary between consequent redshift intervals. This procedure was used to derive an overall FIR luminosity density corrected for incompleteness, which was later compared to the hot-dust regime as explored in Messias et al. (2013).

The LDFs showed that, at $z \sim 1.42$, the Total Population is influenced by the AGN Population in the bright-end. This may be due to hot-dust around AGNs and at temperatures close to that of sublimation, boosting H-band fluxes, causing a shift of some galaxies to the bright-end. In addition, the AGN dust torus emission may be dominating at the observed FIR wavelengths, once again boosting the emission.

The analysis of the LDFs also shows a significance intrinsic evolution in the Total, Late Type, and STB populations, both in the ϕ^* and M^* Schechter parameters. This implies that, the typical FIR emitter at $z \sim 1.42$ is around 3 to 4 times brighter than the typical FIR emitter at $z \sim 0.12$, and emits around 8 to 20 times more in the FIR.

The findings described in this dissertation for the FIR-to-NIR luminosity density ratio with redshift do not corroborate the results in Messias et al. (2013). This means that the lowest redshift bins, which provide smaller cosmological volumes, are highly affected by cosmic variance, which induced the evolution mismatch between the FIR and NIR spectral regimes reported in Messias et al. (2013).

Interestingly, it is found that the FIR-to-NIR luminosity density ratio nicely correlates with H-band luminosity. While the non-AGN populations show an increasing FIR-to-NIR luminosity density ratio with H-band luminosity at all redshifts, the opposite behavior is observed for the AGN population. The latter can simply be understood as a more dominant dust-torus component in the near- to mid-IR spectral regime in the most luminous AGN. The former, however, may require a more complex analysis, since different energy budgets available to heat up the dust in the ISM or even different stellar populations appearing at specific galaxy evolution stages may come to play to induce such a trend.

Due to the lack of data-points for the Early Type and AGN populations, the evolution of the FIR-to-NIR luminosity density ratio for these samples could not be assessed. This is induced by the passive nature of Early Type galaxies resulting in a null detection in the *Herschel* stacking analysis, and due to the low number of AGN host galaxies in the sample at the lowest redshifts, respectively.

4.1 Future Work

Since we believe that the lowest redshift intervals are affected by cosmic variance, it is key to confirm these results in a wider area field which will provide a larger number of objects. This will allow lower statistical errors and confirm or

refute the results, and, in addition, it will provide a more complete view on the Early Type and AGN Populations at low redshift. For this purpose, a combination of the upcoming space-based *Wide-Field Infrared Survey Telescope* (WFIRST; $0.76 - 2\ \mu m$) observations and those already performed by WISE ($3.4 - 4.6\ \mu m$) will be key to achieve this goal.

Finally, it will be of utmost interest to explore the physics behind the correlation found for the non-AGN galaxies between the FIR-to-NIR luminosity density ratio and H-band luminosity. For this purpose, the mbb analysis considered in this study can be further explored to provide a more complete characterization of a given population, for instance, in terms of dust mass. More complex SED fitting algorithms (e.g., Magphys, da Cunha et al. 2008) can be explored to infer other physical properties which may shed light into the reasons behind such a trend. In addition, spectroscopic observations by AKARI of the NIR spectral regime (Imanishi et al. 2010; Yamada et al. 2013) can be used as templates to better characterize this regime.

References and Bibliography

Allamandola, L. J., Tielens, A. G. G. M., Barker, J. R. (1985). *Polycyclic Aromatic Hydrocarbons and the unidentified infrared emission bands: Auto exhaust along the Milky Way!* The Astrophysical Journal, 290:L25-L28.

Allamandola, L. J., Tielens, A. G. G. M., Barker, J. R. (1989). *Interstellar Polycyclic Aromatic Hydrocarbons: the infrared emission bands, the excitation/emission mechanism, and the Astrophysical implications* The Astrophysical Journal Suplement Series, 71:733-775.

Allamandola, L. J., Hudgins, D. M., Sandford, S. A. (1999). *Modeling the unidentified Infrared Emission with combinations of Polycyclic Aromatic Hydrocarbons*. The Astrophysical Journal, 511:L115-L119.

Bernstein, R. A., Freedman, W. L., Madore, B. F. (2002). *The First Detections of the Extragalactic Background Light at 3000, 5500, and 8000 Å. III. Cosmological Implications*. The Astrophysical Journal, 571:107-128.

Bertoldi, F., Carilli, C. L., Cox, P., Fan, X., Strauss, M. A., Beelen, A., Omont, A., Zylka, R. (2003). *Dust emission from the most distant quasars*. A&A 406, L55–L58.

Bianchi, S., Schneider, R. (2007). *Dust formation and survival in supernova ejecta*. Mon. Not. R. Astron. Soc. 378, 973–982.

Biviano, A. (1998). *Our best friend, the Coma cluster (a historical review)*. A. Mazure, F. Casoli, F. Durret, & D. Gerbal, ed., Untangling Coma Berenices: A New Vision of an Old Cluster, p1.

Boulanger, F., Pérault, M. (1988). *Diffuse infrared emission from the galaxy. I - Solar neighborhood*. The Astrophysical Journal, 330:964-985.

Boyer, M. L., Srinivasan, S., Riebel, D., McDonald, I., van Loon, J. T., Clayton, G. C. et al. (2012). *The dust budget of the Small Magellanic Cloud: are Asymptotic Giant Branch Stars the primary dust source at low metallicity?* The Astrophysical Journal, 748:40 (10pp).

Brandl, B. R., Bernard-Salas, J., Spoon, H. W. W. et al. (2006). *The mid-Infrared properties of Starburst Galaxies from Spitzer-IRS Spectroscopy*. The Astrophysical Journal, 653:1129-1144.

Brusa, M., Civano, F., Comastri, A., Miyaji, T., Salvato, M. et al. (2010). *The XMM-Newton Wide-field Survey in the Cosmos Field (XMM-COSMOS): Demography and Multiwavelength Properties of Obscured and Unobscured Luminous Active Galactic Nuclei*. The Astrophysical Journal, 716:348-369.

Cesarsky, D., Lequeux, J., Abergel, A., Perault, M., Palazzi, E., Madden, S., Tran, D. (1996). *Infrared spectrophotometry of NGC 7023 with ISOCAM*. A&A 315, L305–L308.

Chary, R., Elbaz, D. (2001). *Interpreting the Cosmic Infrared Background: Constraints on the Evolution of the Dust-enshrouded Star Formation Rate*. The Astrophysical Journal, 556:562-581.

Chary, R. R., Pope, A. (2010). *New Observational Constraints and Modeling of the Infrared Background: Dust Obscured Star-Formation at $z > 1$ and Dust in the Outer Solar System*. arXiv:1003.1731v1 [astro-ph.CO].

Cherchneff, I., Dwek, E. (2010). *The chemistry of population III Supernova ejecta. II. The nucleation of molecular clusters as a diagnostic for dust in the early Universe*. The Astrophysical Journal, 713:1–24.

da Cunha, E., Charlot, S., Elbaz, D. (2008). *A simple model to interpret the ultraviolet, optical and infrared emission from galaxies*. Mon. Not. R. Astron. Soc. 388, 1595–1617.

Dale, D. A., Helou, G. (2002). *The Infrared Spectral Energy Distribution of Normal Star-forming Galaxies: Calibration at Far-Infrared and Submillimeter Wavelengths*. The Astrophysical Journal, 576:159–168.

Dey, A., Soifer, B. T., Desai, V., Brand, K., Le Floc'h, E. et al. (2008). *A Significant Population of Very Luminous Dust-Obscured Galaxies at Redshift* $z \sim 2$. The Astrophysical Journal, 677:943-956.

Dole, H., Lagache, G., Puget, J.-L., Caputi, K. I., Fernández-Conde, N. et al. (2006). *The cosmic infrared background resolved by Spitzer. Contributions of mid-infrared galaxies to the far-infrared background*. A&A 451, 417–429.

Dowell, C. D., Conley, A., Glenn, J. et al. (2014). *HerMES: Candidate High-Redshift Galaxies discovered with Herschel/SPIRE*. The Astrophysical Journal, 780:75 (24pp).

Draine, B. T. (2003). *Interstellar Dust Grains*. Annu. Rev. Astron. Astrophys. 2003. 41:241–289.

Draine, B. T. (2009). *Interstellar Dust Models and Evolutionary Implications*. Th. Henning, E. Grün, and J. Steinacker, eds. COSMIC DUST—NEAR AND FAR. ASP Conference Series, Vol. 414, 2009.

Draine, B. T., Lee, H. M. (1984). *Optical properties of interstellar Graphite and Silicate grains*. The Astrophysical Journal, 285:89-108.

Draine, B. T., Li, A. (2001). *Infrared Emission from Interstellar dust. I. Stochastic heating of small grains*. The Astrophysical Journal, 551:807-824.

Draine, B. T., Li, A. (2007). *Infrared Emission from Interstellar dust. IV. The Silicate-Graphite-PAH model in the post-SPITZER era*. The Astrophysical Journal, 657:810-837.

Drory, N., Bundy, K., Leauthaud, A., Scoville, N., Capak, P., Ilbert, O. et al. (2009). *The Bimodal Galaxy Stellar Mass Function in the COSMOS Survey to* $z \sim 1$*: A Steep Faint End and a New Galaxy Dichotomy*. The Astrophysical Journal, 707:1595–1609.

Dullemond, C. P., Monnier, J. D. (2010). *The Inner Regions of Protoplanetary Disks*. Annu. Rev. Astron. Astrophys. 2010. 48:205–239.

Fazio, G. G. et al. (2004). *The Infrared Array Camera (IRAC) for the SPITZER Space Telescope*. The Astrophysical Journal Supplement Series, 154:10–17.

Ferrarotti, A. S., Gail, H.-P. (2006). *Composition and quantities of dust produced by AGB-stars and returned to the interstellar medium*. A&A 447, 553–576.

Foreman-Mackey, D., Hogg, D. W., Lang, D., Goodman, J. (2013). *emcee: The MCMC Hammer*. arXiv:1202.3665v4 [astro-ph.IM].

Fu, H., Yan, L., Scoville, N. Z., Capak, P., Aussel, H., Le Floc'h, E. et al. (2010). *Decomposing Star Formation and Active Galactic Nucleus with Spitzer Mid-infrared Spectra: Luminosity Functions and Co-evolution*. The Astrophysical Journal, 722:653–667.

Greenberg, J. M. (1968). *Interstellar Grains*. Stars and Stellar Systems, Vol. 7, ed. B. M. Middlehurst & L. H. Aller (Chicago: Univ. Chicago Press), 221

Griffin, M.J., Abergel, A., Abreu, A. et al. (2010). *The Herschel-SPIRE instrument and its in-flight performance*. A&A 518, L3.

Henriques, B. M. B., White, S. D. M., Thomas, P. A., Angulo, R., Guo, Q., Lemson, G., Springel, V., Overzier, R. (2015). *Galaxy formation in the Planck cosmology - I. Matching the observed evolution of star formation rates, colours and stellar masses*. Mon. Not. R. Astron. Soc. 451, 2663-2680.

Hillenbrand, L. A., Strom, S. E., Vrba, F. J., Keene, J. (1992). *HERBIG Ae/Be Stars: Intermediate-Mass Stars surrounded by massive circumstellar accretion disks*. The Astrophysical Journal, 397:613-643.

Hollenbach, D. J., Tielens, A. G. G. M. (1997). *Dense Photodissociation Regions (PDRs)*. ARA&A 1997. 35:179-215.

Hönig, S. F., Kishimoto, M. (2010). *The dusty heart of nearby active galaxies. II. From clumpy torus models to physical properties of dust around AGN*. A&A 523, A27.

Houck, J. R., Weedman, D. W., Le Floc'h, E., Lei Hao (2007). *Spitzer Spectra of a 10 mJy Galaxy Sample and the Star Formation Rate in the Local Universe*. The Astrophysical Journal, 671:323-332.

Hubble, E., Humason, M. L. (1931). *The Velocity-Distance Relation among Extra-Galactic Nebulae*. The Astrophysical Journal, 74:43-80.

Hunt, L. K. (2010). *The dusty Universe: astronomy at infrared wavelengths*. Mem. S.A.It. Suppl. Vol. 14, 78.

Ilbert, O., Capak, P.;, Salvato, M., Aussel, H., McCracken, H. J., Sanders, D. B., Scoville, N. et al. (2009). *Cosmos Photometric Redshifts with 30-Bands for* $2\ deg^2$. The Astrophysical Journal, 690:1236–1249.

Imanishi, M., Nakagawa, T., Shirahata, M., Ohyama, Y., Onaka, T. (2010). *AKARI IRC Infrared* $2.5-5\ \mu m$ *Spectroscopy of a Large Sample of Luminous Infrared Galaxies*. The Astrophysical Journal, 721:1233–1261.

Inoue, A. K. (2011). *The origin of dust in galaxies revisited: the mechanism determining dust content*. Earth Planets Space, 63, 1–12, 2011.

Kartaltepe, J. S., Sanders, D. B., Le Floc'h, E., Frayer, D. T. et al. (2010). *A Multiwavelength Study of a Sample of* $70\ \mu m$ *Selected Galaxies in the COSMOS Field. I. Spectral Energy Distributions and Luminosities*. The Astrophysical Journal, 709:572-596.

Knobel, C., Lilly, S. J., Iovino, A., Kovač, K., Bschorr, T. J., Presotto, V., Oesch, P. A. et al. (2012). *The zCOSMOS 20k Group Catalog*. The Astrophysical Journal, 753:121 (24pp).

Krumholz, M. R. (2012). *Star Formation in Atomic Gas*. The Astrophysical Journal, 759:9 (9pp).

Krumholz, M. R., McKee, C. F., Tumlinson, J. (2008). *The Atomic-to-Molecular Transition in Galaxies. I. An Analytic Approximation for Photodissociation Fronts in Finite Clouds*. The Astrophysical Journal, 689:865-882.

Lau, R. M., Herter, T. L., Morris, M. R., Li, Z., Adams, J. D. (2015). *Old supernova dust factory revealed at the Galactic center*. Science 24 Apr 2015: Vol. 348, Issue 6233, pp. 413-418.

Le Floc'h, E., Papovich, C., Dole, H., Bell, E. F., Lagache, G., Rieke, G. H. et al. (2005). *Infrared Luminosity Functions from the Chandra Deep Field-South: The Spitzer View on the History of Dusty Star Formation at* $0 \lesssim z \lesssim 1$. The Astrophysical Journal, 632:169–190.

Léger, A., D'Hendecourt, L., Défourneau, D. (1989). *Physics of IR emission by interstellar PAH molecules*. A&A 216,148-164.

Leger, A., Puget, J. L. (1984). *Identification of the "unidentified" IR emission features of interstellar dust?* A&A 137,L5-L8.

Levenson, L., Marsden, G., Zemcov, M. et al. (2010). *HerMES: SPIRE Science Demonstration Phame Maps*. arXiv:1010.0020v1 [astro-ph.CO].

Lilly, S. J., Le Brun, V., Maier, C., Mainieri, V., Mignoli, M. et al. (2009). *The zCOSMOS 10k-Bright Spectroscopic Sample*. The Astrophysical Journal Supplement Series, 184:218–229.

Lonsdale, Carol J.; Lacy, M.; Kimball, A. E.; Blain, A.; Whittle, M.; Wilkes, B. et al. (2015). *Radio Jet Feedback and Star Formation in Heavily Obscured, Hyperluminous Quasars at Redshifts* $\sim 0.5 - 3$. *I. ALMA Observations*. The Astrophysical Journal, 813:45 (26pp).

Lutz, D. (2014). *Far-infrared surveys of galaxy evolution*. Annu. Rev. Astron. Astrophys. 2014 52.

Lutz, D., Poglitsch, A., Altieri, B. et al. (2011). *PACS Evolutionary Probe (PEP) - A Herschel Key Program*. arXiv:1106.3285v1 [astro-ph.CO].

Madden, S. C., Galliano, F., Jones, A. P., Sauvage, M. (2006). *ISM properties in low-metallicity environments*. A&A 446, 877–896.

Magnellis, B., Elbaz, D., Chary, R. R., Dickinson, M., Le Borgne, D., Frayer, D. T., Willmer, C. N. A. (2009). *The* $0.4 < z < 1.3$ *star formation history of the Universe as viewed in the far-infrared*. A&A 496, 57–75.

Mathis, J. S., Rumpl, W., Nordsieck, K. H. (1977). *The size distribution of interstellar grains*. The Astrophysical Journal, 217:425-433.

Messias, H. (2011). *A multiwavelength study of near- and mid-infrared selected galaxies at high redshift: ERGs, AGN-identification and the contribution from dust*. PhD Thesis, Faculdade de Ciências da Universidade de Lisboa, Lisboa, Portugal.

Messias, H., Afonso, J., Salvato, M., Mobasher, B., Hopkins, A. M. (2012). *A New Infrared Color Criterion for the Selection of* $0 < z < 7$ *AGNs: Application to Deep Fields and Implications for JWST Surveys*. The Astrophysical Journal, 754:120 (16pp).

Messias, H., Mobasher, B., Afonso, J. (2013). *Hot-dust (690 K) luminosity density and its evolution in the last 7.5 Gyr*. The Astrophysical Journal, 776:117 (12pp).

Michałowski, M. J., Murphy, E. J., Hjorth, J., Watson, D., Gall, C., Dunlop, J. S. (2010). *Dust grain growth in the interstellar medium of* $5 < z < 6.5$ *quasars*. A&A 522, A15.

Mitchell-Wynne, K., Santos, M. G., Afonso, J., Jarvis, M. J. (2014). *Beyond stacking: a maximum-likelihood method to constrain radio source counts below the detection threshold*. Mon. Not. R. Astron. Soc. 437, 2270-2278.

Mobasher, B., Trentham, N. (1998). *Near-infrared luminosity function and colours of dwarf galaxies in the Coma cluster*. Mon. Not. R. Astron. Soc. 293, 315–324.

Morgan, H. L., Edmunds, M. G. (2003). *Dust formation in early galaxies*. Mon. Not. R. Astron. Soc. 343, 427–442.

Nenkova, M., Sirocky, M. M., Ivezić, Ž., Elitzur, M. (2008). *AGN Dusty Tori I. Handling of Clumpy Media*. The Astrophysical Journal, 685:147–159.

Neugebauer, G., Habing, H. J., van Duinen, R. et al. (1984). *The Infrared Astronomical Satellite (IRAS) Mission*. The Astrophysical Journal, 278:L1–L6.

Nozawa, T., Kozasa, T., Umeda, H., Maeda, K., Nomoto, K. (2003). *Dust in the early Universe: Dust formation in the ejecta of Population III Supernovae*. The Astrophysical Journal, 598:785–803.

Oliver, S. J., Bock, J., Altieri, B. et al. (2012). *The Herschel Multi-tiered Extragalactic Survey: HerMES*. arXiv:1203.2562v1 [astro-ph.CO].

Pilbratt, G. L., Riedinger, J. R., Passvogel, T. et al. (2010). *Herschel Space Observatory - An ESA facility for far-infrared and submillimetre astronomy*. A&A 518, L1.

Pirronello, V., Liu, C., Shen, L., Vidali, G. (1997). *Laboratory Synthesis of Molecular Hydrogen on Surfaces of Astrophysical Interest*. The Astrophysical Journal, 475:L69–L72.

Pirronello, V., Biham, O., Liu, C., Shen, L., Vidali, G. (1997). *Efficiency of Molecular Hydrogen Formation on Silicates*. The Astrophysical Journal, 483: L131–L134.

Pirronello, V., Liu, C., Roser, J. E., Vidali, G. (1999). *Measurements of molecular hydrogen formation on carbonaceous grains*. A&A 344, 681–686.

Poglitsch, A., Waelkens, C., Geis, N. et al. (2010). *The Photodetector Array Camera and Spectrometer (PACS) on the Herschel Space Observatory*. A&A 518, L2.

Rapacioli, M., Joblin, C., Boissel, P. (2005). *Spectroscopy of Polycyclic Aromatic Hydrocarbons and very small grains in photodissociation regions*. A&A 429, 193–204.

Riechers, D. A., Bradford, C. M., Clements, D. L., Dowell, C. D., Pérez-Fournon, I. et al. (2013). *A dust-obscured massive maximum-starburst galaxy at a redshift of 6.34*. Nature 496, 329–333.

Rowlands, K., Gomez, H. L., Dunne, L., Aragón-Salamanca, A., Dye, S., Maddox, S., da Cunha, E., van der Werf, P. (2013). *The dust budget crisis in high-redshift submillimetre galaxies*. Mon. Not. R. Astron. Soc. 000, 1–20.

Salvato, M., Ilbert, O., Hasinger, G., Rau, A., Civano, F., Zamorani, G., Brusa, M. et al. (2011). *Dissecting Photometric Redshift for Active Galactic Nucleus Using XMM- and Chandra-COSMOS Samples*. The Astrophysical Journal, 742:61 (15pp).

Sanders, D. B., Salvato, M., Aussel, H., Ilbert, O., Scoville, N. et al. (2007). *S-COSMOS: The Spitzer Legacy Survey of the Hubble Space Telescope ACS* $2\ deg^2$ *COSMOS Field I: Survey Strategy and First Analysis*. The Astrophysical Journal Supplement Series, 172:86–98.

Schechter, P. (1975). *The luminosity function for galaxies and the clustering of galaxies*. Ph.D. thesis, California Institute of Technology, Pasadena, CA USA.

Schechter, P. (1976). *An analytic expression for the luminosity function for galaxies*. The Astrophysical Journal, 203:297-306.

Scoville, N., Aussel, H., Brusa, M., Capak, P. et al. (2007). *The Cosmic Evolution Survey (COSMOS): Overview*. The Astrophysical Journal Supplement Series, 172:1–8.

Sellgren, K. (1984). *The Near-Infrared continuum emission of visual reflection Nebulae*. The Astrophysical Journal, 277:623–633.

Sellgren, K., Werner, M. W., Dinerstein, H. L. (1983). *Extended near-infrared emission from visual reflection nebulae*. The Astrophysical Journal, 271:L13–L17.

Smith, J. D. T., Draine, B. T., Dale, D. A. et al. (2007). *The mid-Infrared Spectrum of star-forming Galaxies: Global Properties of Polycyclic Aromatic Hydrocarbon emission*. The Astrophysical Journal, 656:770-791.

Tielens, A. G. G. M. (2008). *Interstellar Polycyclic Aromatic Hydrocarbon Molecules*. Annu. Rev. Astron. Astrophys. 2008. 46:289–337.

Todini, P., Ferrara, A. (2001). *Dust formation in primordial Type II supernovae*. Mon. Not. R. Astron. Soc. 325, 726-736.

Trump, J. R., Impey, C. D., Elvis, M., McCarthy, P. J., Huchra, J. P. et al. (2009). *The COSMOS Active Galactic Nucleus Spectroscopic Survey. I. XMM-Newton Counterparts*. The Astrophysical Journal, 696:1195–1212.

Trumpler, R. J. (1930). *Absorption of Light in the Galactic System*. Publ. Astron. Soc. Pac. 42:214–27.

Valiante, R., Schneider, R., Salvadori, S., Bianchi, S. (2011). *The origin of the dust in high-redshift quasars: the case of SDSS J1148+5251*. Mon. Not. R. Astron. Soc. 416, 1916–1935.

Verstraete, L., Puget, J. L., Falgarone, E., Drapatz, S., Wright, C. M., Timmermann, R. (1996). *SWS spectroscopy of small grain features across the M17-Southwest photodissociation front*. A&A 315, L337–L340.

Vieira, J. D., Marrone, D. P., Chapman, S. C., De Breuck, C., Hezaveh, Y. D. et al. (2013). *Dusty starburst galaxies in the early Universe as revealed by gravitational lensing*. Nature 495, 344–347.

Viero, M. P., Wang, L., Zemcov, M. et al. (2013). *HerMES: Cosmic Infrared Background anisotropies and the clustering of dusty Star-forming Galaxies*. arXiv:1208.5049v3 [astro-ph.CO].

Viero, M. P., Moncelsi, L., Quadri, R. F., Arumugam, V., Assef, R. J. et al. (2013). *HerMES: The Contribution to the Cosmic Infrared Background from Galaxies Selected by Mass and Redshift*. The Astrophysical Journal, 779:32 (23pp).

Weedman, D. W., Houck, J. R. (2008). *The Most Luminous Starbursts in the Universe*. The Astrophysical Journal, 686:127–137.

Wright, E. L. (2006). *A Cosmological Calculator for the World Wide Web*. Publ. Astron. Soc. Pac. 118:1711-1715.

Wu, Y., Charmandaris, V., Hao, L., Brandl, B. R., Bernard-Salas, J., Spoon, H. W. W., Houck, J. R. (2006). *Mid-Infrared Properties of Low-Metallicity Blue Compact Dwarf Galaxies from the Spitzer Infrared Spectrograph*. The Astrophysical Journal, 639:157–172.

Yamada, R., Oyabu, S., Kaneda, H., Yamagishi, M., Ishihara, D., Kim, J. H., Im, M. (2013). *A Relation of the PAH* $3.3\ \mu m$ *Feature with Star-forming Activity for Galaxies with a Wide Range of Infrared Luminosity*. PASJ: Publ. Astron. Soc. Japan 65, 103.

Zafar, T., Watson, D. (2013). *The metals-to-dust ratio to very low metallicities using GRB and QSO absorbers; extremely rapid dust formation*. A&A 560, A26.

Appendix A

Modified Black Body Fit and Stack Images for each Population and Redshift

The mbb fits mentioned in Section 2.2 are shown here.

Each figure illustrates a population. In it, the mbb fit for each redshift bin is represented, as well as the stacking results at each wavelength (100, 160, 250, 350, and 500 μm) in the same order of the points in the graphic.

The red points mean that the signal significance is smaller than 3σ for that stack image, and were, therefore, considered non-detections. The green points indicate the signal significance is greater than 3σ for that stack image, and are considered detections.

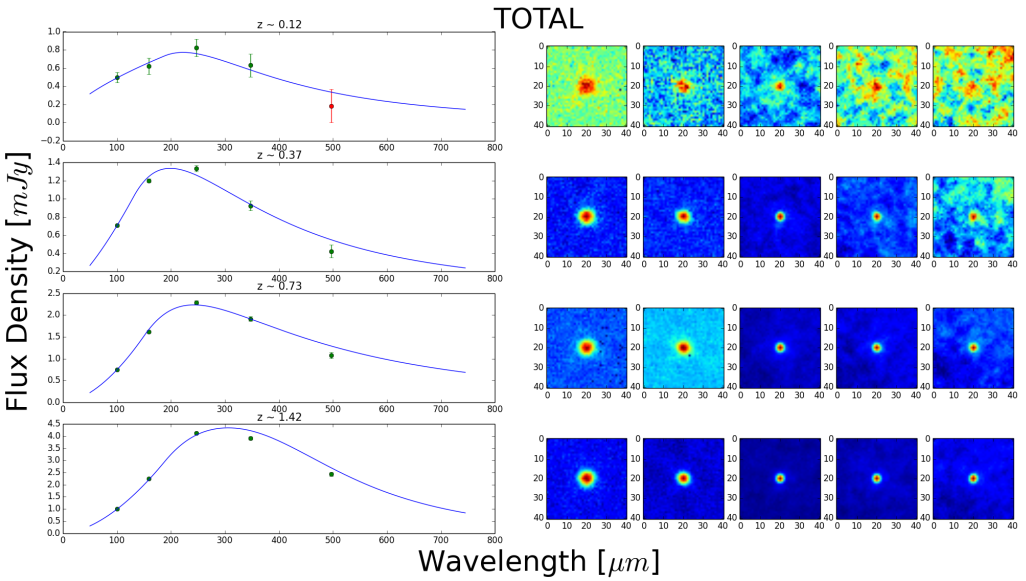

Figure A.1: Results of the mbb fit and stamps for the Total Population.

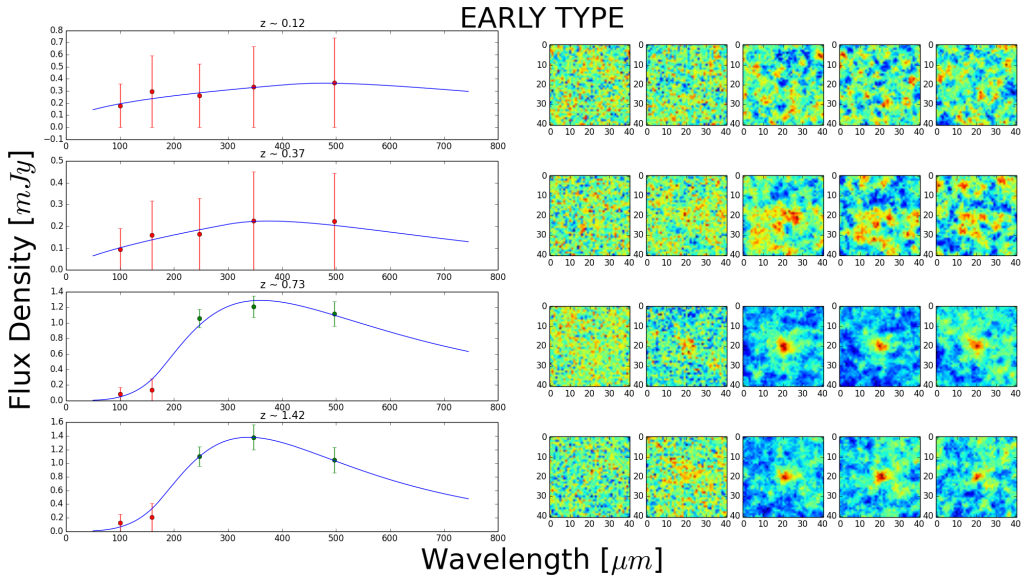

Figure A.2: Results of the mbb fit and stamps for the Early Type Population.

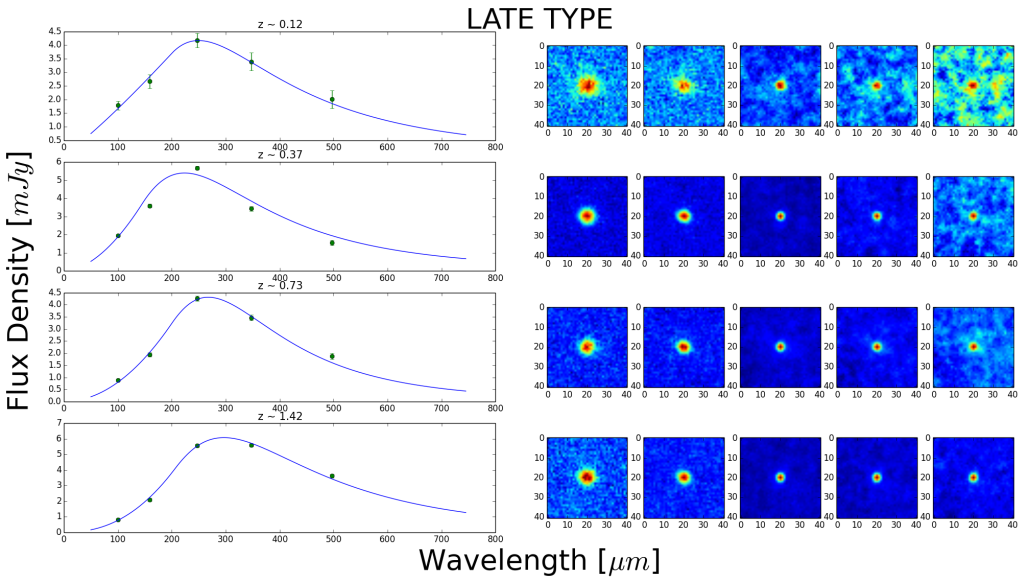

Figure A.3: Results of the mbb fit and stamps for the Late Type Population.

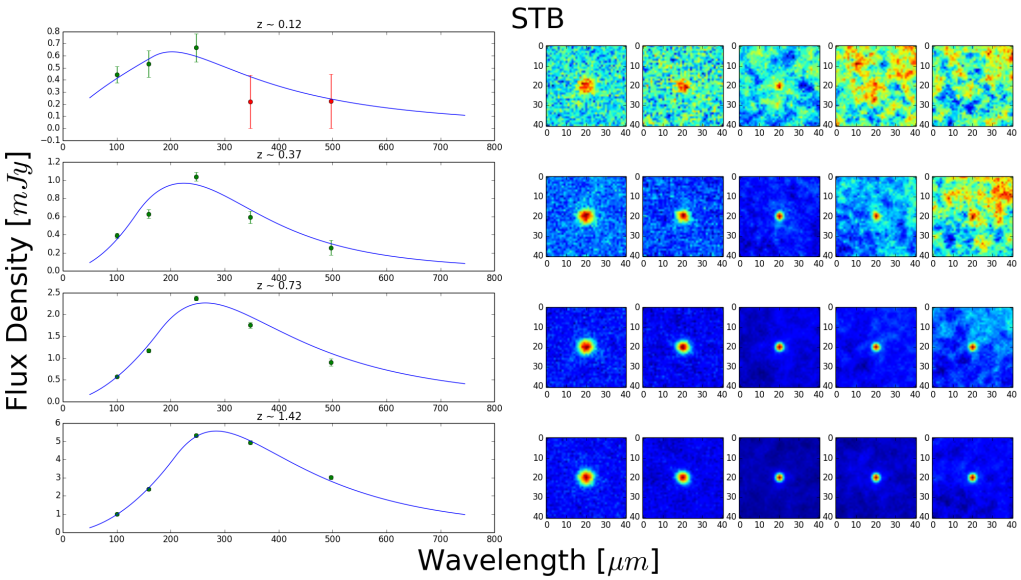

Figure A.4: Results of the mbb fit and stamps for the STB Population.

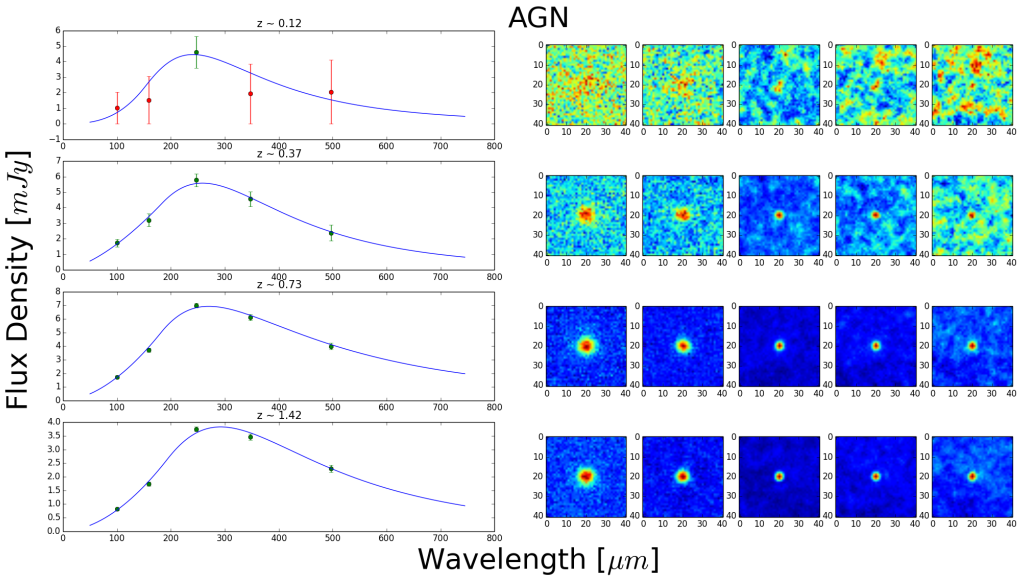

Figure A.5: Results of the mbb fit and stamps for the AGN Population.

Appendix B

Modified Black Body Fit and Stack Images for each Population, Redshift, and Magnitude

The mbb fits mentioned in Section 2.3 are shown here.

Each figure illustrates a population and a redshift bin, except for the Early Type Population, since there was less detections for that population. In it, the mbb fit for each magnitude bin is represented, as well as the stacking results at each wavelength (100, 160, 250, 350, and 500 μm) in the same order of the points in the graphic.

The red points mean that the signal significance is smaller than 3σ for that stack image, and were, therefore, considered non-detections. The green points indicate the signal significance is greater than 3σ for that stack image, and are considered detections.

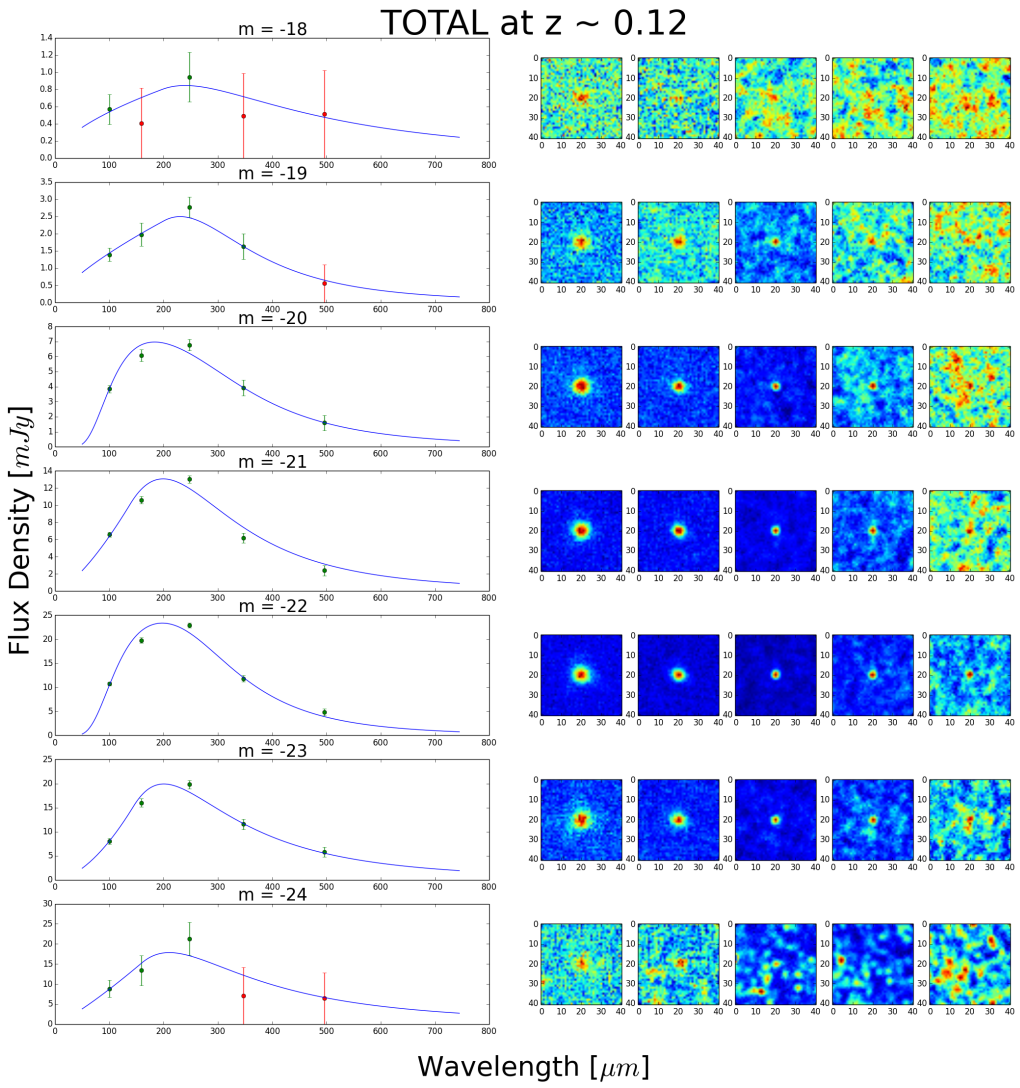

Figure B.1: Results of the mbb fit and stamps for the Total Population at $z \sim 0.12$.

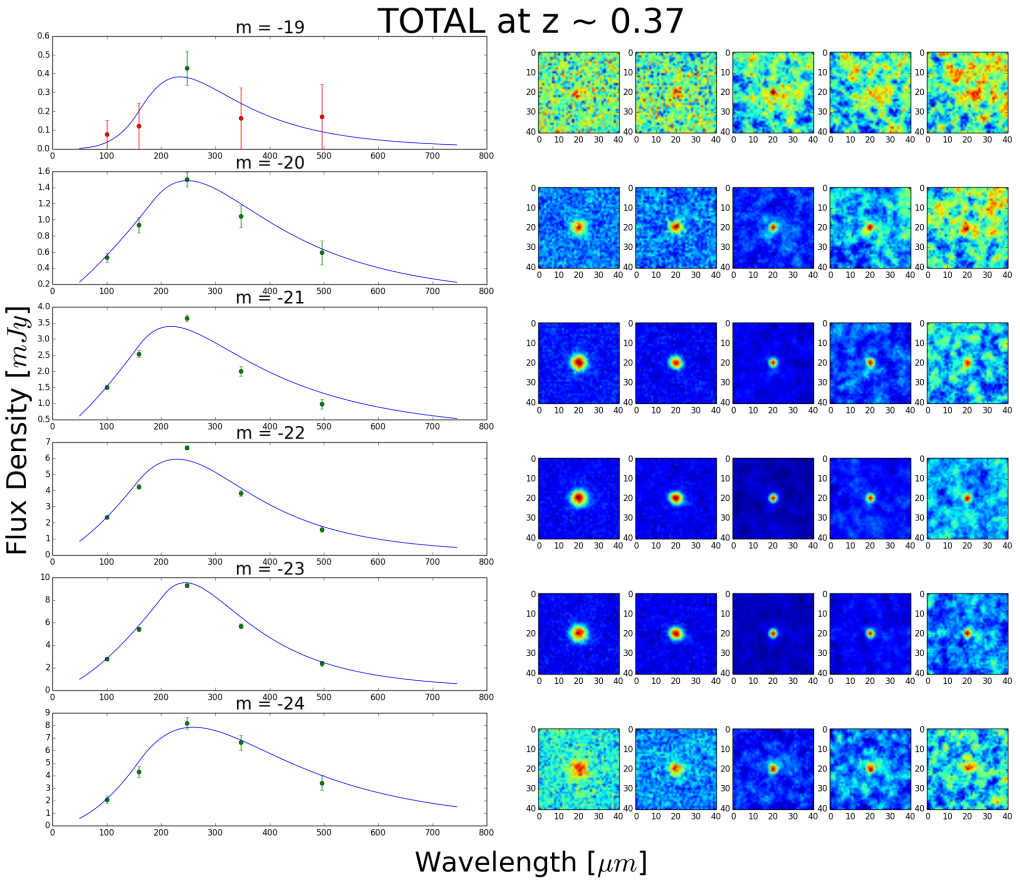

Figure B.2: Results of the mbb fit and stamps for the Total Population at $z \sim 0.37$.

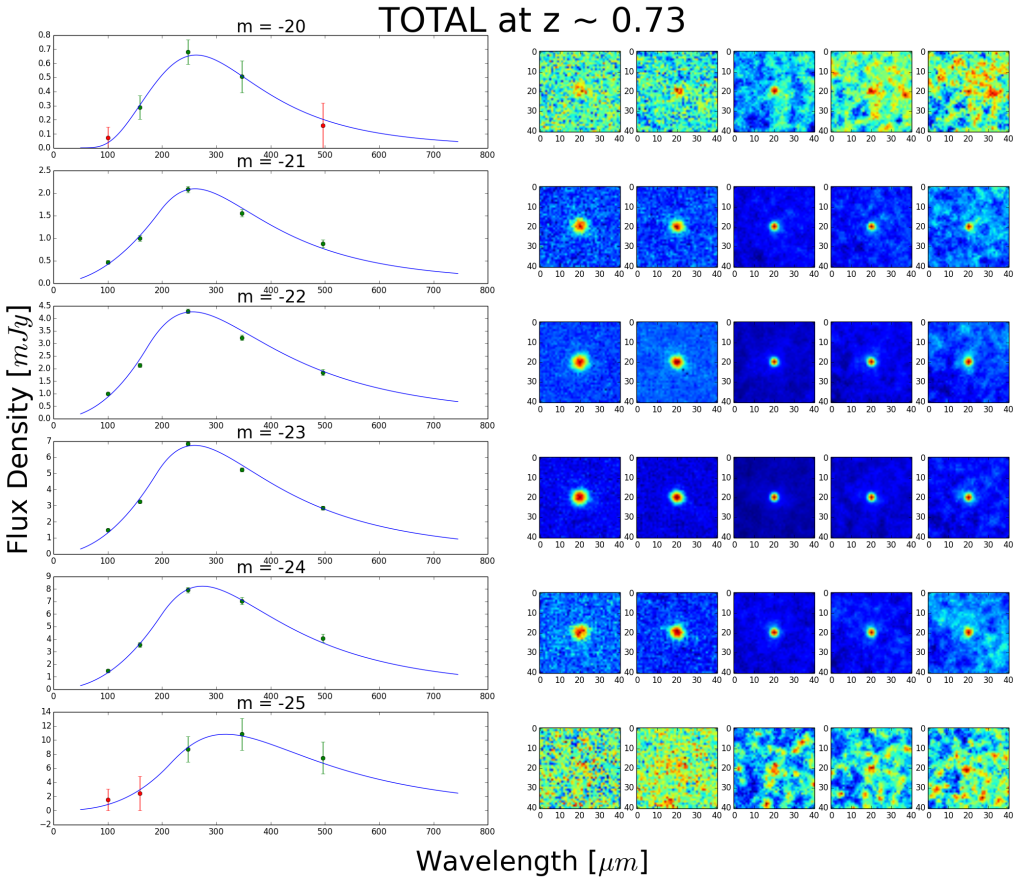

Figure B.3: Results of the mbb fit and stamps for the Total Population at $z \sim 0.73$.

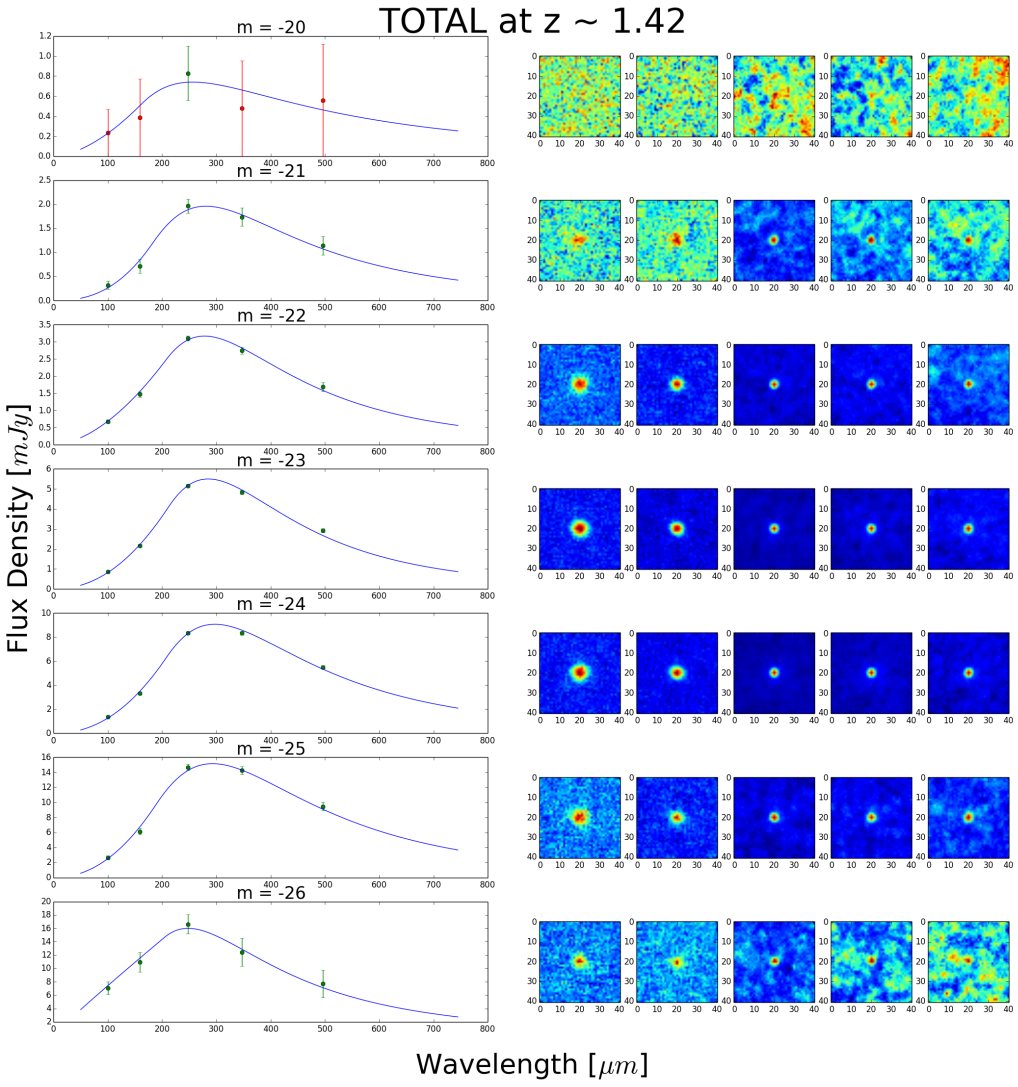

Figure B.4: Results of the mbb fit and stamps for the Total Population at $z \sim 1.42$.

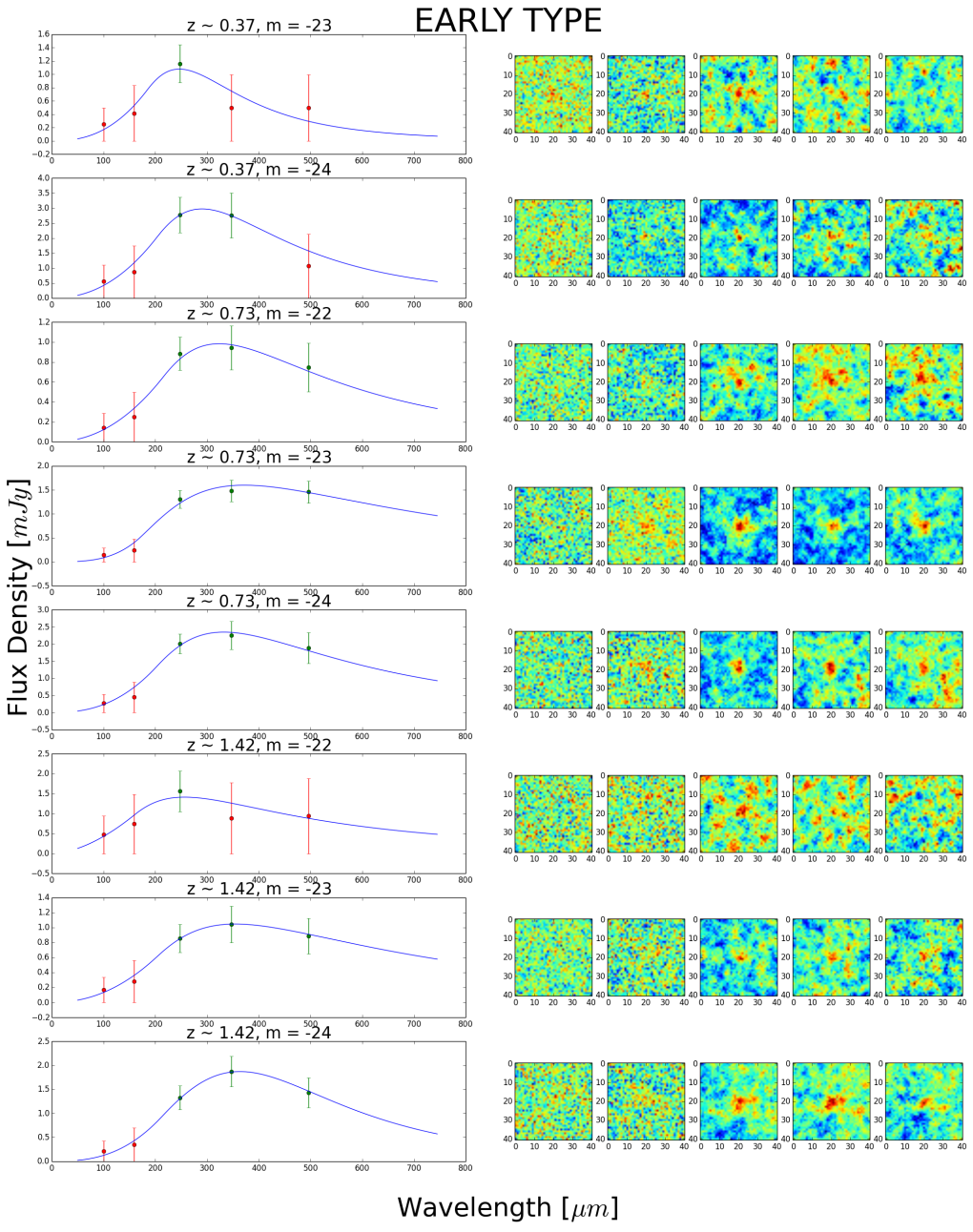

Figure B.5: Results of the mbb fit and stamps for the Early Type Population.

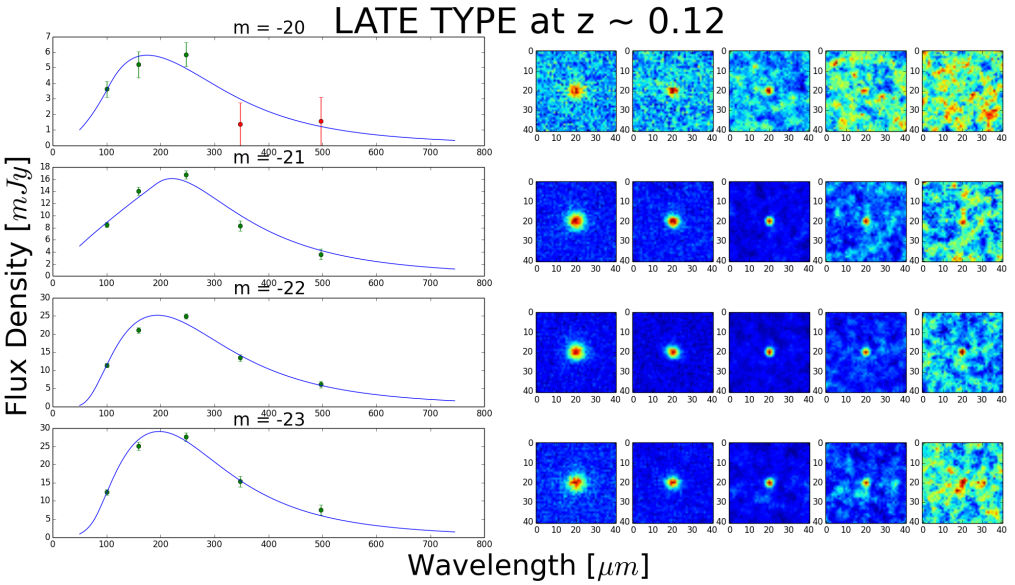

Figure B.6: Results of the mbb fit and stamps for the Late Type Population at $z \sim 0.12$.

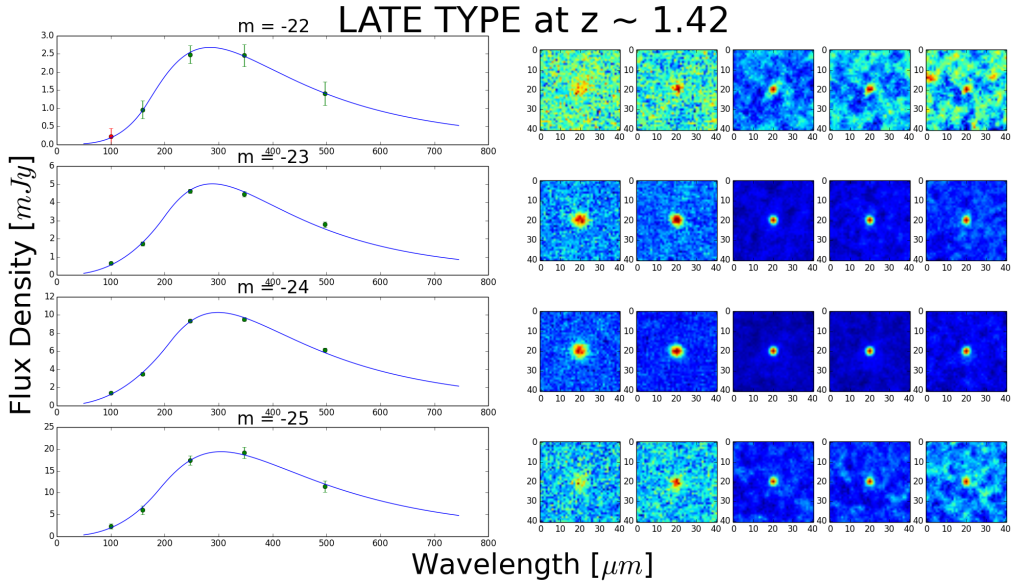

Figure B.7: Results of the mbb fit and stamps for the Late Type Population at $z \sim 1.42$.

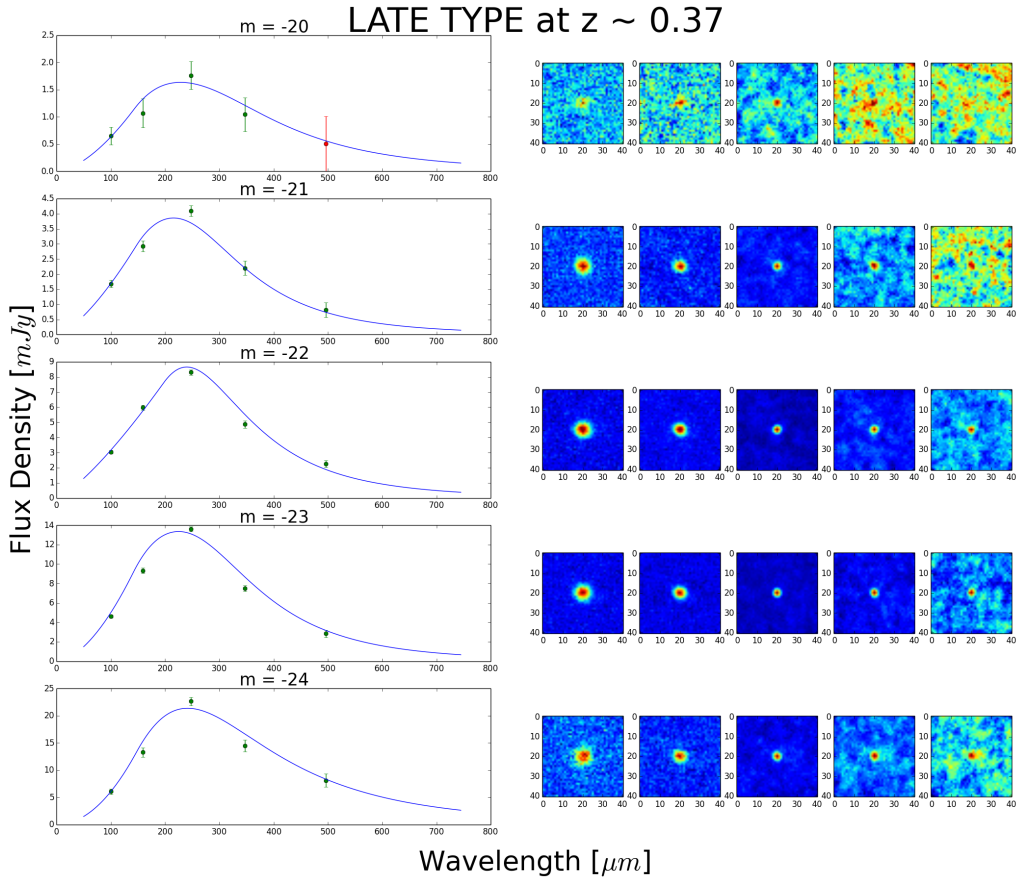

Figure B.8: Results of the mbb fit and stamps for the Late Type Population at $z \sim 0.37$.

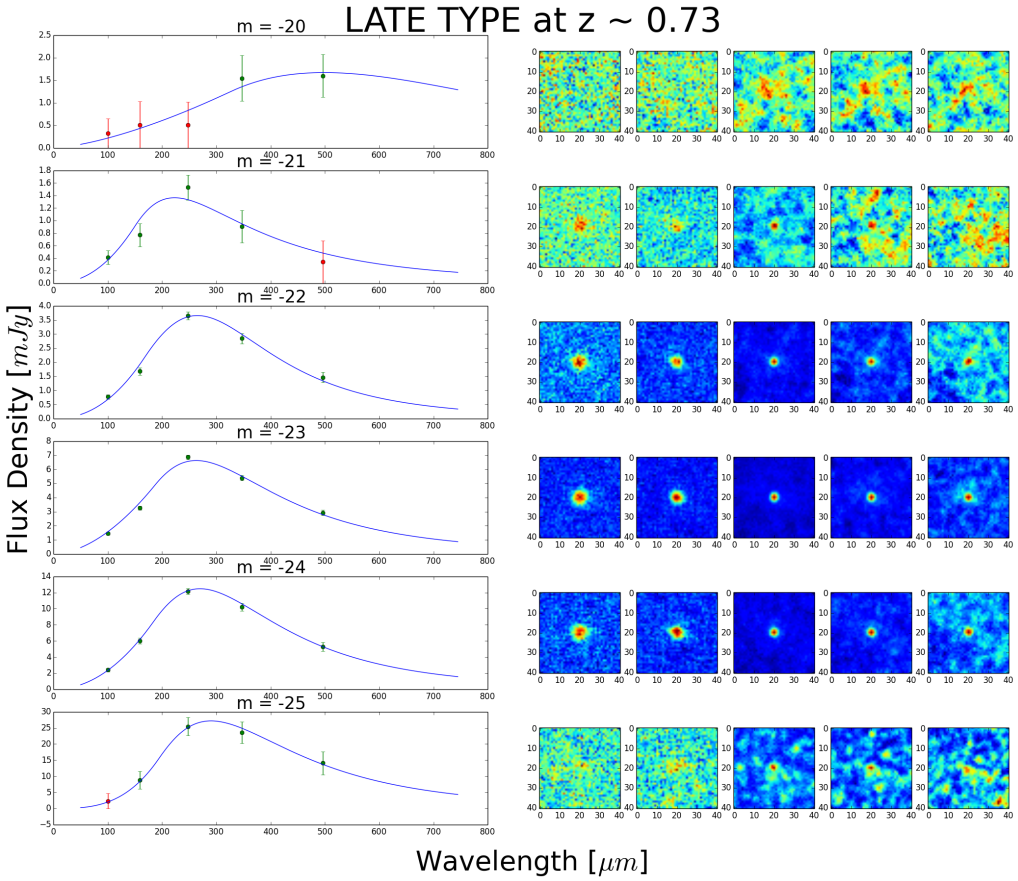

Figure B.9: Results of the mbb fit and stamps for the Late Type Population at $z \sim 0.73$.

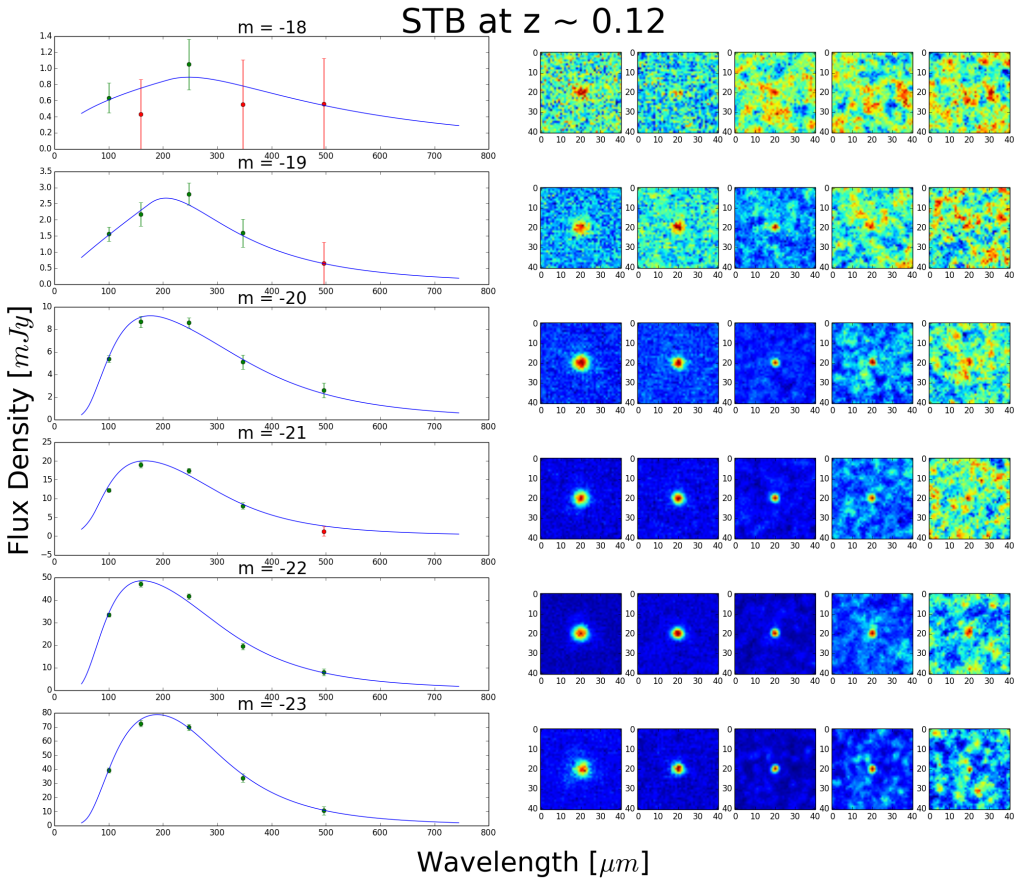

Figure B.10: Results of the mbb fit and stamps for the STB Population at $z \sim 0.12$.

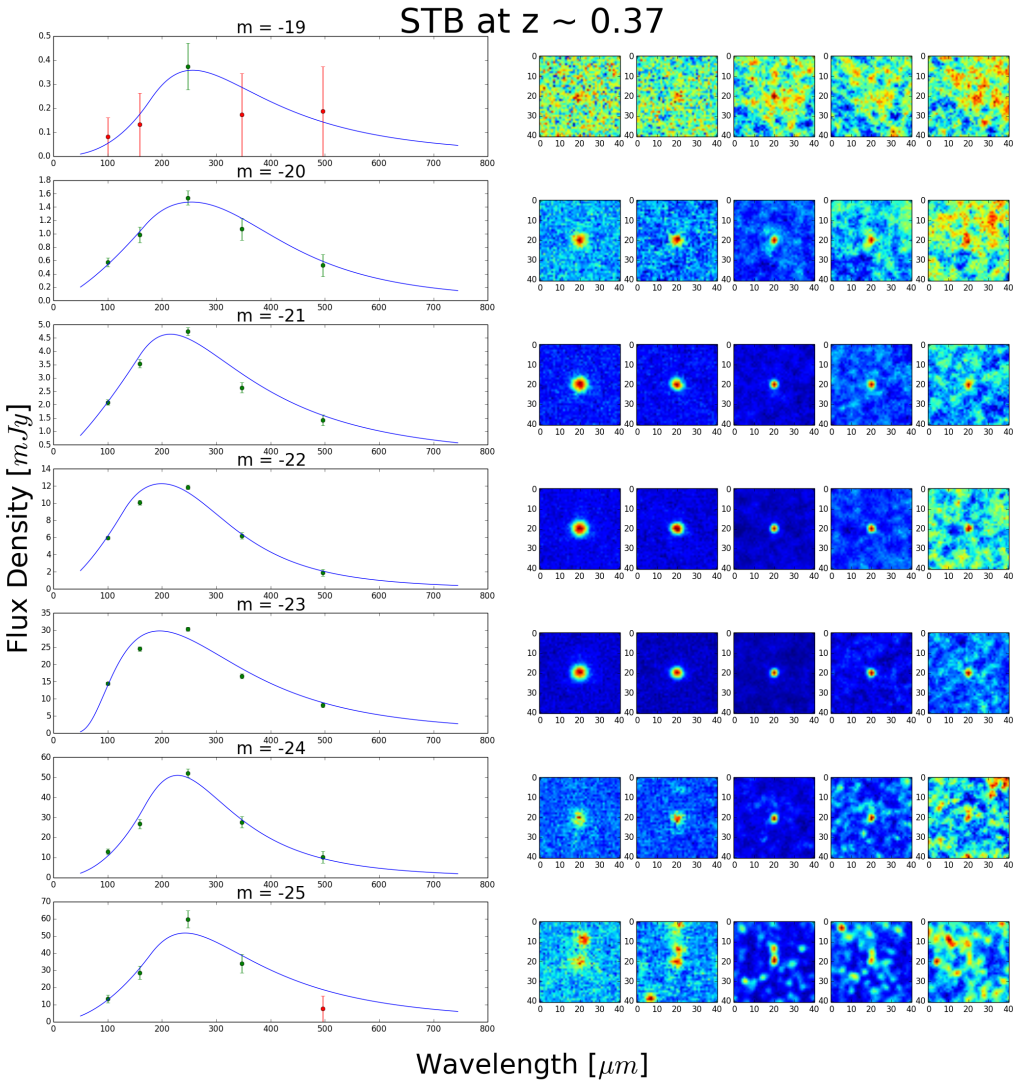

Figure B.11: Results of the mbb fit and stamps for the STB Population at $z \sim 0.37$.

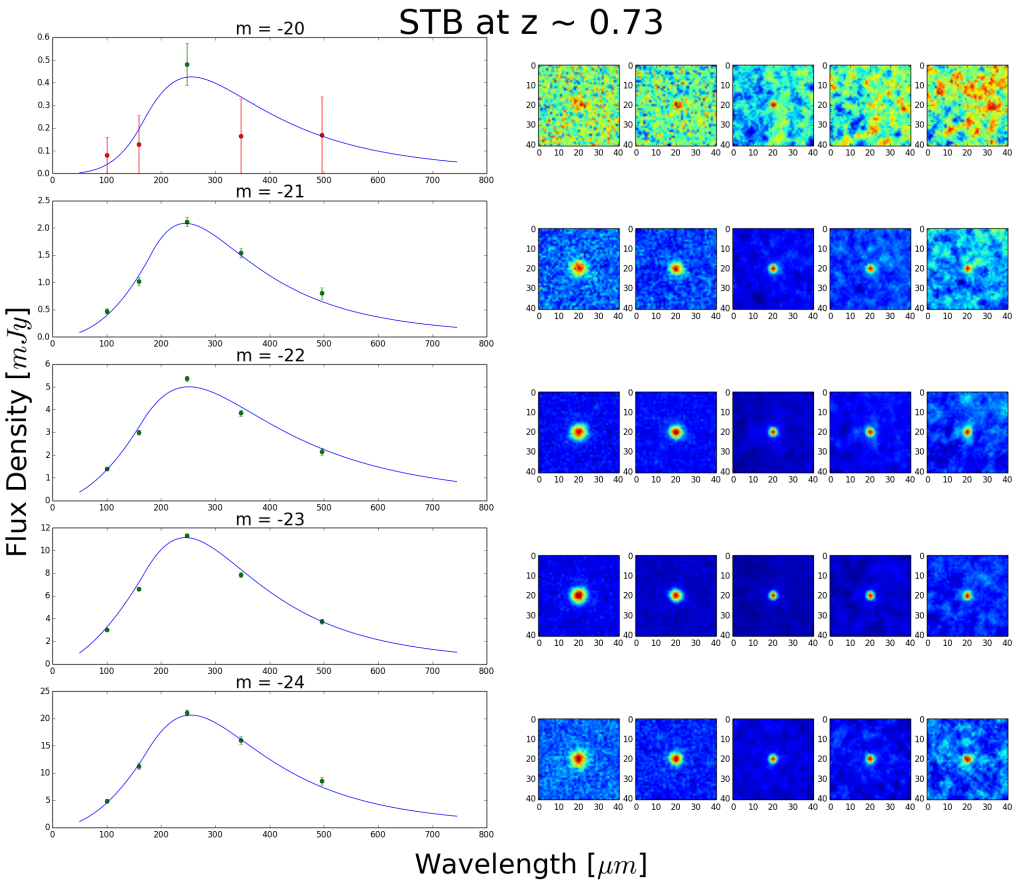

Figure B.12: Results of the mbb fit and stamps for the STB Population at $z \sim 0.73$.

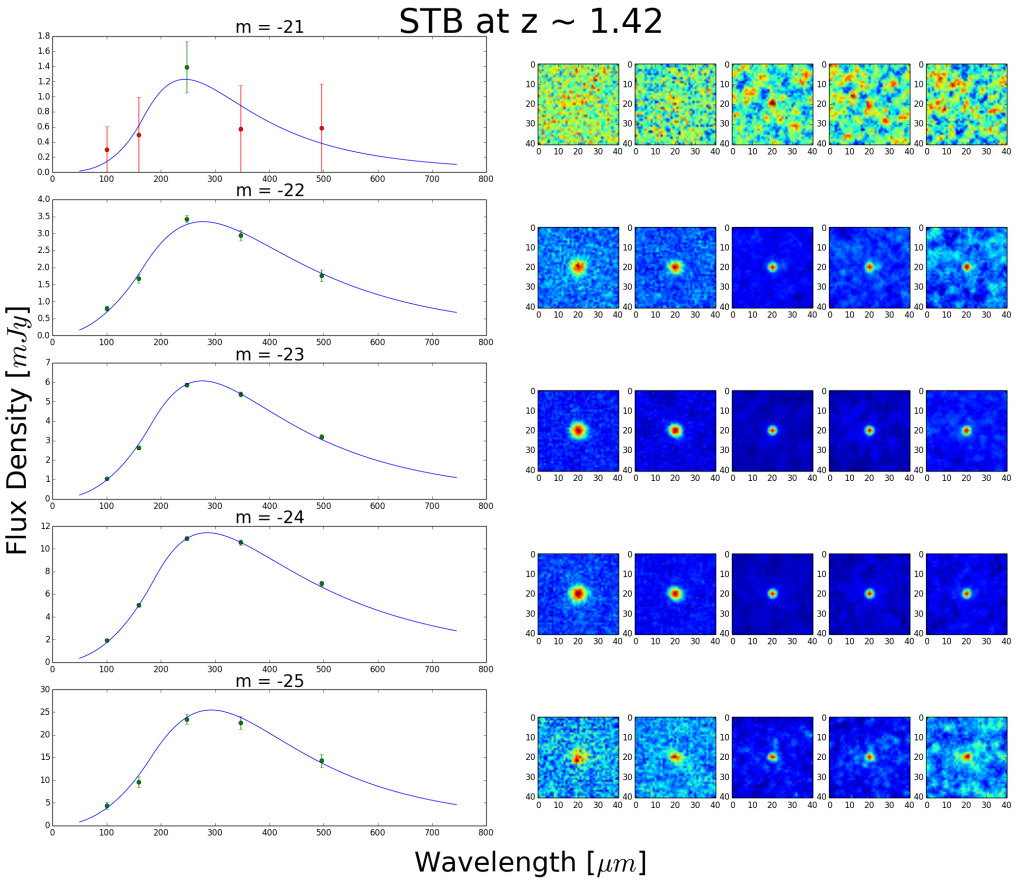

Figure B.13: Results of the mbb fit and stamps for the STB Population at $z \sim 1.42$.

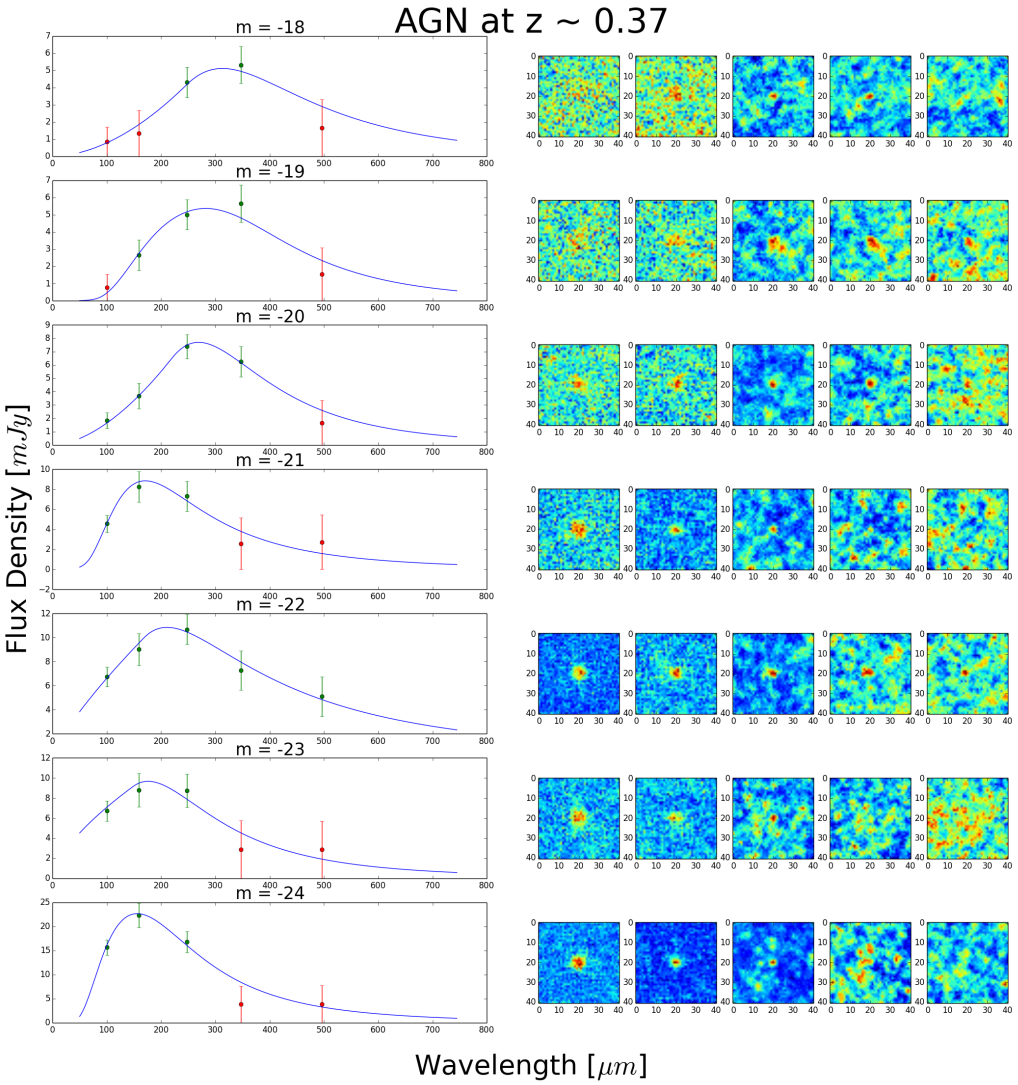

Figure B.14: Results of the mbb fit and stamps for the AGN Population at $z \sim 0.37$.

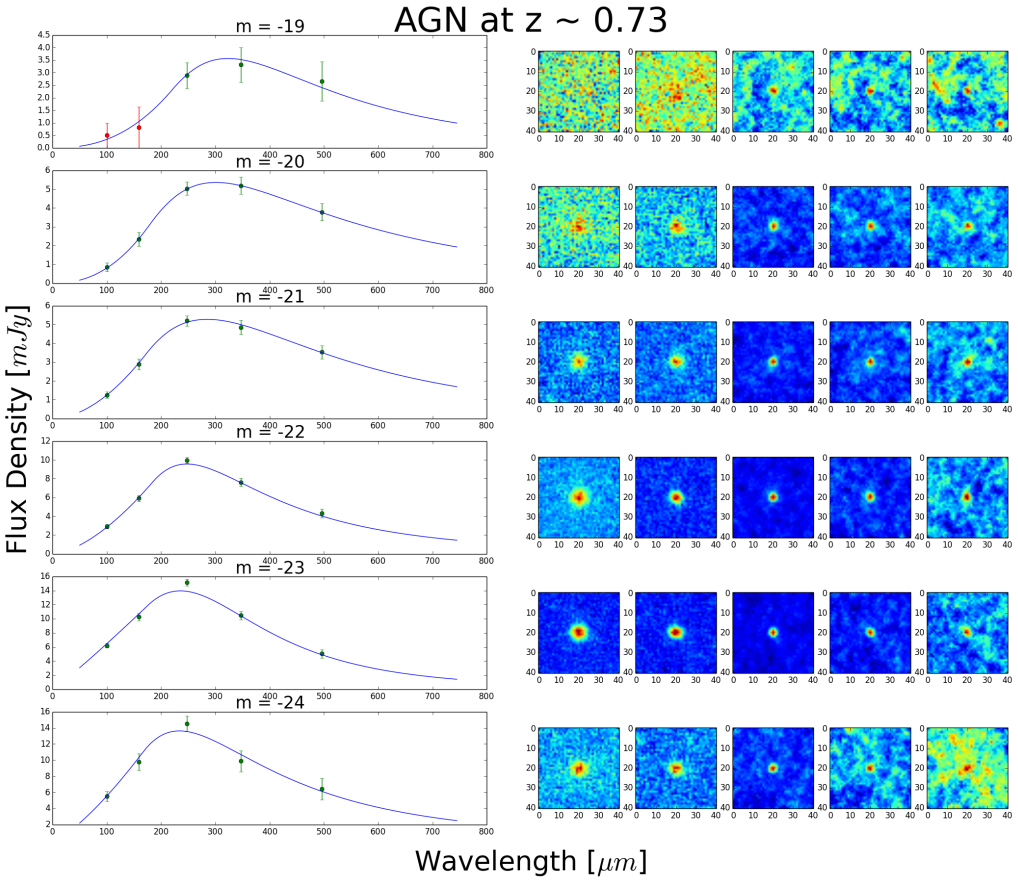

Figure B.15: Results of the mbb fit and stamps for the AGN Population at $z \sim 0.73$.

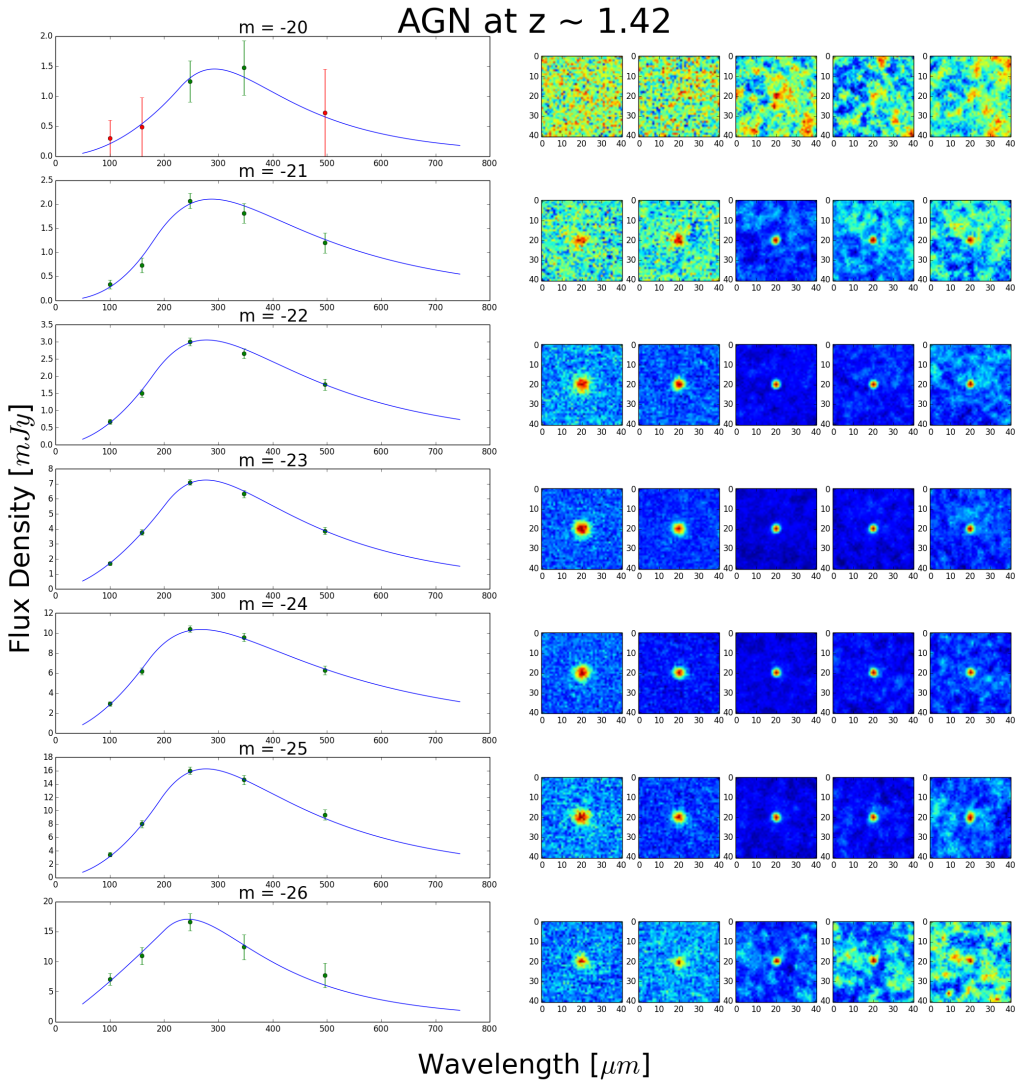

Figure B.16: Results of the mbb fit and stamps for the AGN Population at $z \sim 1.42$.

Appendix C

Far-infrared and Near-infrared Luminosity Density results with Magnitude

The FIR and NIR luminosity density results with absolute magnitude bin are shown here. These results are presented in the logarithmic scale. The tables are divided in each redshift bin.

M_H is the H-band absolute magnitude bin, "LD" is the Luminosity Density, "Tot" represents the Total Population, "Ear" is the Early Type Population, and "Lat" is the Late Type Population. All the luminosity densities are presented in $erg\ s^{-1}Hz^{-1}Mpc^{-3}mag^{-1}$ units.

M_H	LD_{FIR}^{Tot}	LD_{NIR}^{Tot}	LD_{FIR}^{Ear}	LD_{NIR}^{Ear}	LD_{FIR}^{Lat}	LD_{NIR}^{Lat}	LD_{FIR}^{STB}	LD_{NIR}^{STB}	LD_{FIR}^{AGN}	LD_{NIR}^{AGN}
-24.5	$26.31^{0.10}_{0.10}$	-	-	-	-	-	-	-	-	-
-23.5	$27.91^{0.09}_{0.09}$	$23.97^{0.41}_{0.71}$	-	-	$27.08^{0.09}_{0.09}$	$23.83^{0.44}_{0.77}$	$27.70^{0.09}_{0.09}$	-	-	-
-22.5	$28.39^{0.09}_{0.09}$	$25.52^{0.12}_{0.22}$	-	$24.11^{0.34}_{0.67}$	$28.11^{0.09}_{0.09}$	$25.05^{0.16}_{0.31}$	$28.19^{0.09}_{0.09}$	$25.18^{0.21}_{0.37}$	-	-
-21.5	$28.30^{0.09}_{0.09}$	$25.52^{0.08}_{0.14}$	-	$24.48^{0.17}_{0.32}$	$28.01^{0.09}_{0.09}$	$25.14^{0.11}_{0.21}$	$28.13^{0.09}_{0.09}$	$25.21^{0.13}_{0.22}$	-	-
-20.5	$28.20^{0.09}_{0.09}$	$25.36^{0.07}_{0.12}$	-	$24.27^{0.16}_{0.28}$	$27.30^{0.09}_{0.09}$	$24.76^{0.14}_{0.26}$	$28.18^{0.09}_{0.09}$	$25.17^{0.09}_{0.15}$	-	-
-19.5	$27.97^{0.09}_{0.09}$	$25.20^{0.05}_{0.10}$	-	$24.02^{0.17}_{0.30}$	-	$24.53^{0.14}_{0.25}$	$27.91^{0.09}_{0.09}$	$25.03^{0.06}_{0.11}$	-	-
-18.5	$27.58^{0.09}_{0.09}$	$25.05^{0.05}_{0.09}$	-	$23.97^{0.12}_{0.22}$	-	$23.86^{0.28}_{0.49}$	$27.60^{0.09}_{0.09}$	$24.96^{0.05}_{0.09}$	-	$23.69^{0.52}_{0.81}$
-17.5	-	$24.91^{0.04}_{0.07}$	-	$23.99^{0.09}_{0.17}$	-	$23.72^{0.35}_{0.65}$	-	$24.78^{0.04}_{0.07}$	-	$23.75^{0.27}_{0.43}$
-16.5	-	$24.72^{0.04}_{0.06}$	-	$23.87^{0.08}_{0.13}$	-	$23.35^{0.22}_{0.36}$	-	$24.61^{0.04}_{0.07}$	-	$22.83^{0.47}_{0.74}$

Table C.1: Luminosity densities with magnitude bin at $z \sim 0.12$ in units of in $erg\ s^{-1}Hz^{-1}Mpc^{-3}mag^{-1}$ presented in a logarithmic scale.

M_H	LD_{FIR}^{Tot}	LD_{NIR}^{Tot}	LD_{FIR}^{Ear}	LD_{NIR}^{Ear}	LD_{FIR}^{Lat}	LD_{NIR}^{Lat}	LD_{FIR}^{STB}	LD_{NIR}^{STB}	LD_{FIR}^{AGN}	LD_{NIR}^{AGN}
-25.5	-	-	-	-	-	-	$26.87^{0.09}_{0.09}$	-	-	-
-24.5	$27.78^{0.09}_{0.09}$	$25.16^{0.27}_{0.53}$	$26.85^{0.09}_{0.09}$	-	$27.76^{0.09}_{0.09}$	$23.75^{0.28}_{0.55}$	$27.34^{0.09}_{0.09}$	-	$27.12^{0.16}_{0.16}$	$25.04^{0.48}_{0.77}$
-23.5	$28.66^{0.09}_{0.09}$	$25.68^{0.05}_{0.09}$	$27.04^{0.09}_{0.09}$	$24.76^{0.10}_{0.20}$	$28.54^{0.09}_{0.09}$	$25.27^{0.05}_{0.10}$	$28.43^{0.09}_{0.09}$	$25.08^{0.11}_{0.19}$	$27.10^{0.16}_{0.16}$	$24.68^{0.36}_{0.61}$
-22.5	$28.84^{0.09}_{0.09}$	$26.00^{0.02}_{0.04}$	-	$25.12^{0.04}_{0.08}$	$28.67^{0.09}_{0.09}$	$25.66^{0.03}_{0.05}$	$28.62^{0.09}_{0.09}$	$25.51^{0.04}_{0.07}$	$27.41^{0.16}_{0.16}$	$24.73^{0.21}_{0.34}$
-21.5	$28.82^{0.09}_{0.09}$	$25.91^{0.02}_{0.03}$	-	$24.80^{0.04}_{0.07}$	$28.29^{0.09}_{0.09}$	$25.41^{0.03}_{0.05}$	$28.75^{0.09}_{0.09}$	$25.67^{0.02}_{0.04}$	$27.16^{0.16}_{0.16}$	$24.19^{0.20}_{0.33}$
-20.5	$28.59^{0.09}_{0.09}$	$25.66^{0.02}_{0.03}$	-	$24.39^{0.05}_{0.09}$	$27.59^{0.09}_{0.09}$	$24.78^{0.04}_{0.07}$	$28.54^{0.09}_{0.09}$	$25.53^{0.02}_{0.03}$	$27.44^{0.16}_{0.16}$	$24.37^{0.15}_{0.24}$

Table C.2: Luminosity densities with magnitude bin at $z \sim 0.37$ in units of in $erg\ s^{-1}Hz^{-1}Mpc^{-3}mag^{-1}$ presented in a logarithmic scale.

M_H	LD^{Tot}_{FIR}	LD^{Tot}_{NIR}	LD^{Ear}_{FIR}	LD^{Ear}_{NIR}	LD^{Lat}_{FIR}	LD^{Lat}_{NIR}	LD^{STB}_{FIR}	LD^{STB}_{NIR}	LD^{AGN}_{FIR}	LD^{AGN}_{NIR}
-25.5	$26.77^{0.09}_{0.09}$	-	-	-	$26.78^{0.09}_{0.09}$	-	-	-	-	-
-24.5	$28.65^{0.09}_{0.09}$	$25.81^{0.08}_{0.15}$	$27.46^{0.09}_{0.09}$	$24.60^{0.07}_{0.14}$	$28.34^{0.09}_{0.09}$	$25.05^{0.08}_{0.14}$	$28.32^{0.09}_{0.09}$	$24.82^{0.15}_{0.27}$	$27.81^{0.16}_{0.16}$	$25.49^{0.16}_{0.25}$
-23.5	$29.33^{0.09}_{0.09}$	$26.30^{0.02}_{0.04}$	$27.84^{0.09}_{0.09}$	$25.21^{0.03}_{0.05}$	$28.85^{0.09}_{0.09}$	$25.69^{0.02}_{0.04}$	$29.17^{0.09}_{0.09}$	$25.89^{0.03}_{0.04}$	$28.44^{0.16}_{0.16}$	$25.66^{0.08}_{0.13}$
-22.5	$29.37^{0.09}_{0.09}$	$26.26^{0.01}_{0.02}$	$27.62^{0.09}_{0.09}$	$25.03^{0.03}_{0.06}$	$28.63^{0.09}_{0.09}$	$25.54^{0.02}_{0.04}$	$29.27^{0.09}_{0.09}$	$26.04^{0.01}_{0.02}$	$28.54^{0.16}_{0.16}$	$25.40^{0.06}_{0.10}$

Table C.3: Luminosity densities with magnitude bin at $z \sim 0.73$ in units of in $erg\ s^{-1}Hz^{-1}Mpc^{-3}mag^{-1}$ presented in a logarithmic scale.

M_H	LD_{FIR}^{Tot}	LD_{NIR}^{Tot}	LD_{FIR}^{Ear}	LD_{NIR}^{Ear}	LD_{FIR}^{Lat}	LD_{NIR}^{Lat}	LD_{FIR}^{STB}	LD_{NIR}^{STB}	LD_{FIR}^{AGN}	LD_{NIR}^{AGN}
-26.5	$27.49^{0.09}_{0.09}$	$25.59^{0.25}_{0.41}$	-	-	-	-	-	-	$27.49^{0.16}_{0.16}$	$25.59^{0.25}_{0.41}$
-25.5	$28.54^{0.09}_{0.09}$	$25.88^{0.09}_{0.15}$	-	-	$27.66^{0.09}_{0.09}$	-	$27.73^{0.09}_{0.09}$	-	$28.39^{0.16}_{0.16}$	$25.85^{0.09}_{0.15}$
-24.5	$29.37^{0.09}_{0.09}$	$26.17^{0.03}_{0.05}$	$27.56^{0.09}_{0.09}$	$24.41^{0.07}_{0.13}$	$28.91^{0.09}_{0.09}$	$25.44^{0.03}_{0.05}$	$29.06^{0.09}_{0.09}$	$25.50^{0.03}_{0.06}$	$28.63^{0.16}_{0.16}$	$25.90^{0.05}_{0.09}$
-23.5	$29.60^{0.09}_{0.09}$	-	$27.50^{0.09}_{0.09}$	-	$28.87^{0.09}_{0.09}$	-	$29.41^{0.09}_{0.09}$	-	$28.97^{0.16}_{0.16}$	-

Table C.4: Luminosity densities with magnitude bin at $z \sim 1.42$ in units of in $erg\ s^{-1}Hz^{-1}Mpc^{-3}mag^{-1}$ presented in a logarithmic scale.